



Machine learning for alloys

Gus L. W. Hart¹✉, Tim Mueller², Cormac Toher^{1,3,4} and Stefano Curtarolo^{1,3,4}✉

Abstract | Alloy modelling has a history of machine-learning-like approaches, preceding the tide of data-science-inspired work. The dawn of computational databases has made the integration of analysis, prediction and discovery the key theme in accelerated alloy research. Advances in machine-learning methods and enhanced data generation have created a fertile ground for computational materials science. Pairing machine learning and alloys has proven to be particularly instrumental in pushing progress in a wide variety of materials, including metallic glasses, high-entropy alloys, shape-memory alloys, magnets, superalloys, catalysts and structural materials. This Review examines the present state of machine-learning-driven alloy research, discusses the approaches and applications in the field and summarizes theoretical predictions and experimental validations. We foresee that the partnership between machine learning and alloys will lead to the design of new and improved systems.

Machine learning (ML) has been transforming materials science. The past two decades have been marked by a dramatic increase in the amount of generated data, and ML provides the essential tools to extract information^{1–3}: software that helps in making inferences on materials is now commonplace and often freely available^{1,4}. As a result, there has been a widespread improvement in scientists' ability to develop fundamental understanding, explain experimental results and conduct atomic-scale modelling at unprecedented timescales and length scales. It is increasingly common to automate research by using machine-learned models to suggest new experiments or simulations. The resulting machine-driven feedback loop of data generation, model retraining and improved prediction represents a paradigm shift in materials research.

Applications of ML in computational alloy modelling range from model-Hamiltonian building to data-centric materials science⁵. The former typically focuses on a single material system and requires high-fidelity characterizations. The latter intelligently searches through known results and asks broad questions across a large set of candidates⁴. All applications depend on materials representation, one of the most important concepts in ML^{6–12}. Representation, the mathematical depiction of a material, can be a direct description of the crystal structure or a somewhat broad and indirect description, ignoring many details (such as a list of elements, composition, atomic environments or connectivity). The representation components are commonly referred to as features and serve as the inputs. An ideal representation has four main desiderata.

- Invariance. A representation not respecting all the symmetries of the system (non-invariant) requires more training data because the model must learn

through the output what was incorrectly fed to the input.

- Uniqueness. A unique representation guarantees that no two materials have the same features. A non-unique representation cannot be inverted to generate structures, and the degeneracy in the representation leads to errors in a machine-learned function for at least one of the materials with degenerate features. Despite these problems, many successful representations are not unique^{10,13}.
- Stability. In a deformation-stable representation, two materials that are merely minor distortions of each other have very similar features. An unstable representation makes the problem needlessly difficult, essentially asking for an interpolation of a discontinuous quantity. Uniqueness and stability are difficult to obtain: many well-known representations possess neither of these properties^{7,13–15}.
- Interpretability. An interpretable representation informs the user of the reasons behind the algorithm's predictions^{3,16–18}. Interpretability helps to reveal fundamental insights into the problem and rationalize design principles. Despite its importance, this characteristic is often neglected, owing to implementation difficulties^{19,20}.

Here, we provide an overview of ML concepts, approaches and results relevant to metal alloys: atomic-scale mixtures of two or more species, where at least one is a metal and the global character of the mixture is metallic^{21,22}. This Review consists of three sections. First, the concepts of model-Hamiltonian building and data-centric materials science are briefly summarized, followed by an overview of computational databases, examples of structural representations and approaches

¹Department of Physics and Astronomy, Brigham Young University, Provo, UT, USA.

²Department of Materials Science and Engineering, Johns Hopkins University, Baltimore, MD, USA.

³Center for Autonomous Materials Design, Duke University, Durham, NC, USA.

⁴Department of Mechanical Engineering and Materials Science, Duke University, Durham, NC, USA.

✉e-mail: gus.hart@byu.edu; stefano@duke.edu

<https://doi.org/10.1038/s41578-021-00340-w>

for searching for descriptors. Second, notable studies are introduced, together with the applications that have already been explored. Metallic glasses, high-entropy alloys, shape-memory alloys, superalloys, alloys for catalysis and alloys for magnetism are included. Third, we discuss ML studies for metallurgical alloy processing, mechanical properties (elasticity, strength, ductility, hardness, toughness, stacking faults, stress hotspots, fatigue and cracking, wear and creep) and thermal properties. An analysis of the many ML-like studies of semiconductor alloys^{23–25} is beyond the scope of this work; for recent reviews, see REFS^{2,26,27}. For a description of ML methods, we refer readers to REFS^{1,2,28–32}.

Approaches

From model Hamiltonians to data-centric materials science

Atomistic thermodynamic modelling yields important materials quantities, provided the energy model is highly accurate (energy differences for many alloy configurations are just a few or a few tens of meV per atom) and fast enough to sufficiently sample the appropriate ensemble. Quantum mechanical methods such as density functional theory (DFT) are accurate and generalizable, but they are often too slow to calculate thermodynamic averages at finite temperature. Surrogate models have been proposed to tackle the problem. Metal alloys present a particular challenge for computational modelling because of their tendency to form disordered solid solutions and the need to properly account for configurational entropy. This problem has been successfully addressed through the use of on-lattice (such as cluster expansions^{33,34}) and off-lattice approaches (such as Gaussian approximation potentials⁹ and atomic cluster expansion¹²) (BOX 1). Note that both approaches can lead to interpretable representations. Cluster expansions provided an early proving ground for the application of ML to materials, and, thus, much of the early work on machine-learned model Hamiltonians was done on alloys.

Although surrogate ab initio models are effective for probing material-specific questions, a different approach is needed for screening a wide variety of candidates. Even before the big-data materials science revolution, there was a substantial body of work in the alloy community (BOX 2). Data mining — the extraction of patterns and information from large amounts of data — is commonly combined with high-throughput computation⁴ and becomes effective in this situation. Typically, a high-fidelity quantum approach is used to calculate a desired target quantity over a very large number of candidates and then the results are screened to find the most promising materials. The best solution needs to be experimentally realizable. Thus, it is fundamental that all possible decompositions can be identified to determine global stability^{35,36}. Recent approaches also try to deal with synthesizability of metastable or disordered phases^{37,38} and latent-heat-driven kinetics³⁹.

The dawn of computational databases

The growth of ML applications in materials science is intrinsically connected to the blooming of databases — experimental (such as the Inorganic Crystal Structure

Database⁴⁰) and computational^{41–44} — and to readily available descriptors. The latter are features or combinations of features correlating with observables, and they can be used to predict complicated properties⁴. With efficient descriptors, the search for new materials and properties within the repositories can be performed with ML methods³¹, or even just with data mining, depending on whether the optimum candidates are already included in the set of calculations. In alloy theory, the formation enthalpy (or Gibbs free energy) is an obvious descriptor for stability. Combined with the cluster expansion technique^{33,34}, it led to a multitude of successful studies. As illustrated in BOX 1, a number of algorithms were developed to choose the optimal cluster configurations: cross-validation⁴⁵, genetic algorithms⁴⁶ and even methods borrowed from signal processing, such as compressive sensing⁴⁷. In addition to structural information (when available), alloys are commonly represented by feature vectors containing composition, often combined with properties of the component elements, such as position in the periodic table, electronegativity, valence electron concentrations, melting and liquidus temperatures, heat capacity, atomic radii and volumes, thermal conductivity and diffusivity, and heat of fusion. In the case of models for the bulk mechanical properties such as tensile strength and hardness, processing conditions such as heat treatment time and temperature, quenching type and cold working processes are also often included as features. Calculated properties of the material itself, such as cohesive energy, density, mixing enthalpy (for example, from the Miedema model), ideal mixing entropy, along with atomic structure information, can also be used to predict quantities that are computationally difficult to obtain, such as elastic moduli^{48,49}.

A strong impetus came from the rapid growth of databases, starting in the early 2000s. Following the spirit of high-throughput combinatorial experimental techniques⁵⁰, ab initio approaches were adapted to generate massive amounts of data⁴ (currently, the AFLOW⁴¹, OQMD⁴², Materials Project⁴³ and NOMAD⁴⁴ repositories contain millions of calculations with hundreds of millions of extracted properties). Databases were used to predict new materials and/or to optimize properties, often with ad hoc descriptors⁴. For example, in 2002, a DFT evolutionary approach able to find the most stable configurations out of quaternary fcc and bcc structures with up to four atoms per cell was proposed⁵¹. In 2003, principal component analysis (PCA) was used to data mine missing information in ab initio libraries of alloys versus structure prototypes⁵². This work also used the eigenvalues of the PCA expansion to inform a self-consistent thermodynamic loop converging to the alloy convex hulls^{52,53}. Also in 2003, a multidimensional Pareto optimization was proposed to determine alloy solutions having low compressibility, high stability and low cost⁵⁴. In 2006, Bayesian parameter estimation⁵⁵ was used to predict the crystal structure of experimental binary alloys from the Pauling File project⁵⁶. Later, in 2011, a maximum-likelihood approach was proposed⁵⁷ to data mine the Inorganic Crystal Structure Database⁴⁰ to discover new compounds through ionic substitutions.

Box 1 | On-lattice and off-lattice models**Lattice-based models**

Lattice-based models treat the problem of modelling configurational disorder discretely (in fixed positions, not necessarily part of a Bravais lattice). The atomic structure of an alloy can often be mapped to a single lattice (fcc, for example) whose sites are ‘decorated’ by two or more kinds of atoms. That configuration of atoms may be a repeating pattern, resulting in a particular crystal structure, or a randomized solid solution. In either case, the atoms are assumed to reside, at least approximately, on the sites of the underlying lattice. The premise that each atom can be directly associated with a corresponding lattice site is often realistic enough that accurate quantitative predictions are possible. Many lattice models consider only interactions within local environments defined by cut-off radii. They are informed by vectors of atomic occupations in discrete positions (for example, the partial-occupation approaches^{269,270}), generating interpretable descriptors that can be combined with machine learning to discover new materials¹²⁹. Lattice models have the advantages of speed and accuracy but the drawbacks of not providing forces and being limited to a single underlying lattice. Approaches to building lattice models include the cluster expansion method^{33,34} and its forerunner, the cluster variation method^{271,272}. Lattice gas models are closely related to cluster expansion and have been used extensively in simulations of surfaces and adsorbates^{273–275}. Despite lattice models having been used for decades, innovation is continuing. A novel ‘low-rank potential’ that expresses atomic environments as tensors was recently introduced¹³¹. Tensor-train compression reduces the number of fitting parameters, making this approach well suited for modelling alloys with a large number of components^{131,134}.

Cluster expansion became a dominant approach to alloy modelling starting in the late 1980s and is still used extensively. The method, incorporating many concepts typically associated with data science today, identifies the most significant terms of a linear expansion of basis functions known as cluster functions, each representing the interaction among atoms in a ‘cluster’, or subset, of lattice sites. In the early stages, the cluster expansion coefficients were found by direct inversion or by standard least-squares regression²⁷⁶. As the method matured, and the number of terms in the expansion (and of data points) changed from a handful to thousands, the regression technique embraced modern data-science approaches, including simulated annealing, genetic algorithms^{46,277–279}, compressive sensing⁴⁷, regularization approaches²⁸⁰, including Bayesian methods^{179,281–283}, and different approaches to both cross-validation^{45,284} and training-set generation^{285–288}. The cluster expansion basis is an effective representation naturally including the invariances: the representations of two symmetrically equivalent configurations are numerically identical. In addition, the representation is stable against small perturbations: if a small number of the atoms in a configuration is exchanged, the related features change by a small amount. Lattice models treat configurational entropy directly and are extremely fast. They can be used in large-scale Monte Carlo simulations to perform thermodynamic averages and search for optimal structures. Vibrational contributions are not typically included in lattice models, owing to increased modelling difficulty²⁸⁹.

Off-lattice models

Off-lattice models extend the applicability of lattice models²⁹⁰ to quantities that inherently rely on the details of the atomic coordinates, such as phonons, structural phase transitions, transport and specific heat. Like the cluster expansion, many off-lattice models encode structural information as a set of local interactions, but they allow atoms to have a continuous range of positions. Many concepts developed for lattice models can be extended off-lattice and then used to map structural information to a variety of material properties¹². The most common type of off-lattice models, interatomic potentials, predict the potential energy (typically assumed to be the electronic ground state energy) as a function of the atomic positions within the Born–Oppenheimer approximation. This function is generally known as the potential energy surface. The models integrate electronic degrees of freedom by coarse graining: the forces between atoms are represented by classical interactions that mimic quantum mechanics. Unlike in lattice models, atomic positions are treated explicitly. Two families of potentials exist: simple, physics-based potentials often having a fixed functional form and adjustable parameters (such as the Lennard-Jones or embedded atom potentials²⁹¹) and general, systematically improvable interatomic potentials (such as smooth overlap of atomic positions (SOAP) or Gaussian approximation potentials^{8,9}, atomic cluster expansions^{11,12,192–296} and neural network potentials^{6,186,297,298}). Symbolic regression approaches^{258,299–302} and graph networks^{20,65,66,303–307} have characteristics that overlap with both the physics-based and systematically improvable potentials. Off-lattice models can take advantage of additional information in the training data, such as the first and second energy derivatives, and, in some cases, can be used in place of a cluster expansion³⁰⁸. Training does not require structures to be fully relaxed (as in cluster expansion), making the procedure significantly faster (however, when modelling on-lattice configurational order with an off-lattice model trained on unrelaxed structures, a full relaxation of each configuration must be performed, whereas on-lattice models directly predict the energy of the relaxed structure)³⁰⁹. The simpler the on-lattice and off-lattice models are, the more benefits they offer: they are typically faster, require less training data and may be more interpretable than more complex models³¹⁰. With the availability of so many different off-lattice models, there does not seem to be a clear winner in terms of accuracy versus efficiency^{311,312}.

Macroscopic properties

Beyond merely predicting the existence of compounds, ML can be trained to directly predict other observable macroscopic properties, such as hardness, ductility, toughness and Curie temperature. In 2009, PCA was used to show that structure maps representing structure–property relationships (electronic features and crystal structure parameters) can be reproduced via data mining⁵⁸. In 2018, a random forest (RF) algorithm was used to address phonon spectral features, heat capacities, vibrational entropies and free energies⁵⁹ to improve

predictions of finite-temperature thermodynamic stability. Models can include alloy processing conditions as part of the feature vector, to predict the processing–microstructure–property^{60,61} and composition–process–property⁶² relationships. The section on materials properties describes several other examples.

Examples of representations for structures

Efficient representations are crucial for ML. For example, in 2014, the averaged partial radial distribution function of pairwise distances between atoms was combined with

kernel ridge regression to predict the electronic density of states at the Fermi level⁶³ (FIG. 1a). Representations based on connectivity are promising. N -grams (histograms of unique coordination environments and edge sequences) are effective in predicting formation energies and electronic band gaps⁶⁴. Neural networks (NNs) have been constructed from graphs with nodes representing atoms in the unit cell and edges representing atom connections, giving local atomic environment representations (FIG. 1b). This method has shown reasonable accuracy for formation energies, electronic band gaps, Fermi levels and elastic properties^{65,66}. Most representations are local, in real space and might be ineffective for characterizing properties in periodic systems (such as delocalized features coming from dispersions in reciprocal space). Property-labelled materials fragments are an example of a descriptor that includes periodicity⁴⁹: after partitioning the crystal structure into atom-centred Voronoi–Dirichlet polyhedra (capturing the local environment), an adjacency matrix of the graph is constructed from the total list of connections, reflecting the periodic global topology (FIG. 1c). ML also includes generative models to design materials, for example, in the ‘variational autoencoders’ technique (FIG. 1d). These mathematical frameworks comprise two deep networks, an encoder and a decoder. The first maps data points to a low-dimensional continuous vector space — the latent

space — while the second maps latent vectors back to data points. Materials optimization, done in the highly simplified continuous latent space, has predicted new metastable vanadium oxides⁶⁷.

Searching for descriptors

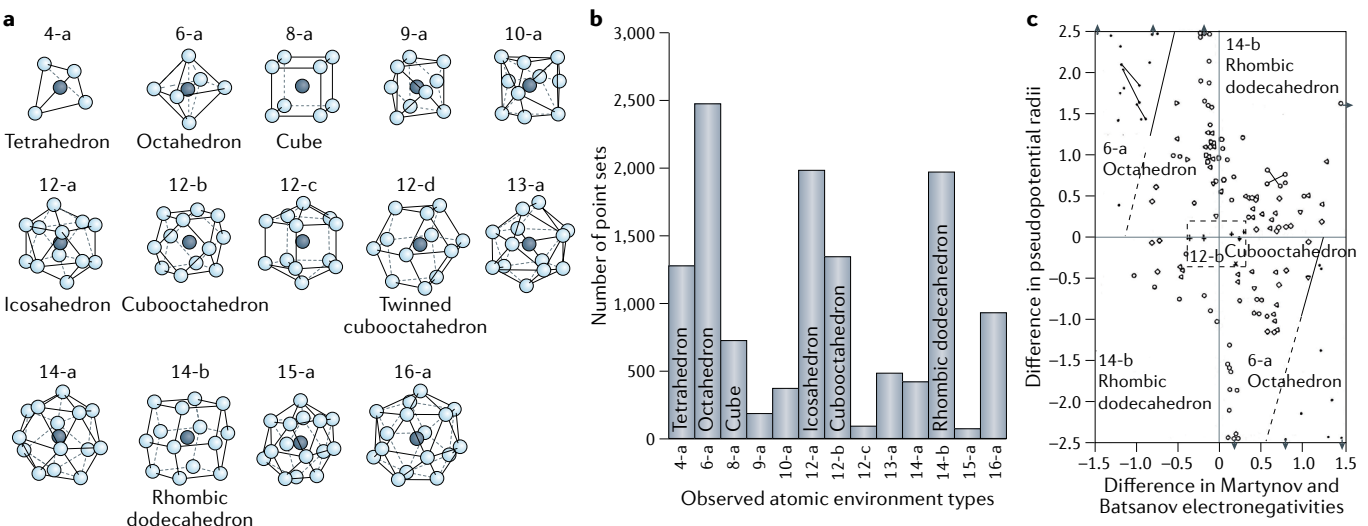
Except in the case of physically motivated descriptors⁴, the ML outcome is an ‘impenetrable box’ connecting input and outputs with optimized internal parameters. Given that descriptors can be combinations of features, several directions have recently been proposed to combine features into (possibly interpretable) functionals.

Starting from a very large set of mathematical operations and their combinations, the space of all constructible formulas can be searched with genetic programming or deterministic optimization. The former leads to stochastic optimization; it is the idea behind the Eureqa framework approach proposed by Michael Schmidt and Hod Lipson in 2009 (REF.⁶⁸) (FIG. 1e). The latter has been explored by LASSO (least absolute shrinkage and selection operator)⁶⁹ and its SISSO evolution (sure independence screening and sparsifying operator)⁷⁰ (FIG. 1f). While not being deterministic, Eureqa has the advantage of being able to span larger feature spaces. LASSO and SISSO seem more efficient and less biased, giving the true optimized descriptor, but the larger computational cost hinders the size of the feature space that can be

Box 2 | When machine learning was done by hand

Alloy research, well positioned to leverage machine learning, has a history of inventing and adopting computational approaches. For decades, researchers have developed new approaches that, if they were to appear today, would be called machine learning. For structure determination, simple prototype clustering was performed quite early. For example, structure maps were proposed by David Pettifor in the 1980s from analysis of experimental databases^{313–315} and later extended in an automatic fashion to computational repositories³¹⁶. The early structure prediction work by Pettifor^{313–315}, followed by that of Alex Zunger³¹⁷, is an illustrative example. Simple atomic features (such as atomic radii, electronegativity, valence electrons and atomic environments) for each element type were used as coordinates to map each candidate material into multidimensional feature spaces. Materials with the same crystal structure tended to cluster together in the feature space. When the crystal structure for a material was as-yet unknown, the proximity to other structures in the map became a prediction.

The figure shows an example of ‘hand-made machine learning’. Panel a shows a phenomenological description of structure as atomic environment: the 14 most frequently occurring atomic environment types are shown with their names. Panel b illustrates a frequency plot of these 14 atomic environments found in 5,086 cubic intermetallics: octahedra, rhombic dodecahedra, icosahedra, cubooctahedra and tetrahedra are the most commonly found environments. Panel c depicts a section of the 3D pseudopotential radius³¹⁸ versus the Martynov and Batsanov electronegativity (square root of the average ionization potential of the valence electrons³¹⁹; the section is given by an averaged number of valence electrons <2.74) for 2,486 single-environment-type compounds (including binary, ternary and quaternary daltonide and berthollide intermetallic compounds). Each symbol indicates a crystal structure. Figure reprinted from REF.³²⁰, Copyright © 2000, John Wiley and Sons.



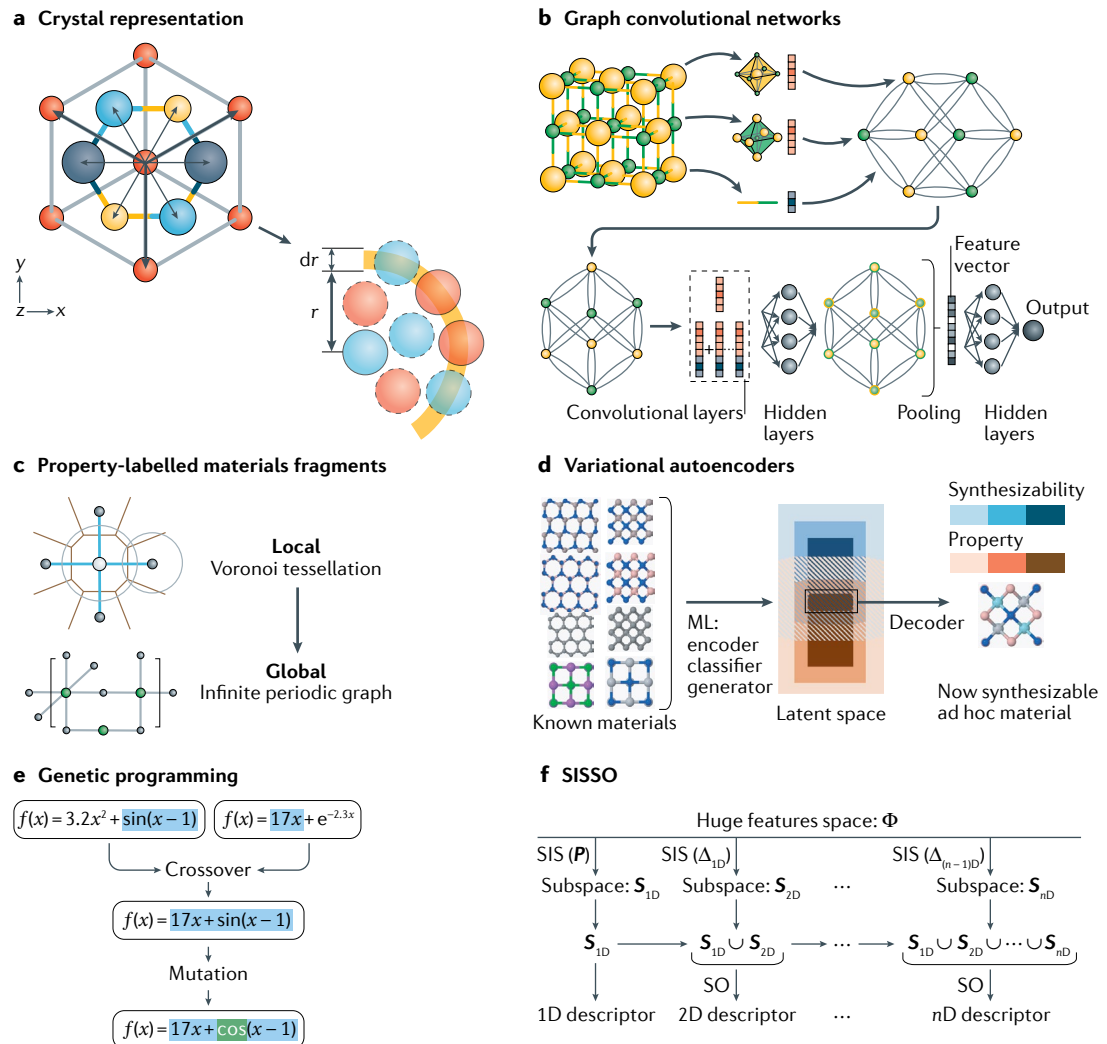


Fig. 1 | Representation of structures and methods for feature selections and descriptors discovery. **a** Alternative crystal representations. Crystal unit cell indicating the Bravais vectors (thick arrows) and base (thin arrows) illustrating one shell of the ‘partial radial distribution function’, the distribution of pairwise distances between the two atomic species (the fraction of atoms of one type in a shell of radius r and width dr centred around an atom of the other type). **b** Crystal graph convolutional neural networks: crystals are converted to graphs with nodes representing atoms in the unit cell and edges representing atom connections. Nodes and edges are characterized by vectors corresponding to the atoms and bonds in the crystal, respectively. The graph is then used to train neural network layers to produce the feature vector of the crystal, followed by the output layer to provide target property prediction. After the first set of hidden layers, a pooling function combines features for each atom into features for the entire crystal. **c** Property-labelled materials fragments include periodicity by connecting local Voronoi tessellation with global periodic graphs. **d** The idea behind variable autoencoders is that the encoder maps data points to a low-dimensional continuous vector space — the latent space — where optimization (for example of properties and synthesizability) is performed, whereas the decoder maps the optimized latent vectors back to data points⁶⁷. **e** Example of possible crossover and mutation steps used to generate new formulas in genetic programming, in which formulas are optimized by an evolutionary algorithm that simulates natural selection. **f** The idea behind SISSO (sure independence screening and sparsifying operator): the iterative deterministic optimization combines unified subspaces having the largest correlation with residual errors generated by sure independence screening (SIS) with the sparsifying operator (SO) to further extract the best descriptor. The target property, P , at the beginning of the cycle is equal to the 0D residual error, Δ_{0D} . Δ is the n -dimensional residual error. ML, machine learning. Panel **a** reprinted with permission from REF.⁶³, APS; panel **b** reprinted with permission from REF.⁶⁵, APS; panel **c** adapted from REF.⁴⁹, CC BY 4.0 (<https://creativecommons.org/licenses/by/4.0/>); panel **e** adapted with permission from REF.²⁶⁸, APS; and panel **f** adapted with permission from REF.⁷⁰, APS.

explored⁷⁰. A more in-depth comparison related to the application in dielectric breakdown strength prediction can be found in REF⁷¹. Recently, there has been an effort to use NNs to accelerate the discovery of formulas. An example is the AI Feynman project⁷², combining the

predictive power of NNs with a brute-force search driven by physically motivated heuristic constraints (such as dimensional analysis, polynomial fit, separability and translational invariance, if appropriate) to perform symbolic regression on a set of pre-established features.

The algorithm seems very promising in rediscovering known formulas⁷²: future extension might include more complicated functional operations (integrals, derivatives) and the capability to search for relevant features within the input data.

Materials families

This section provides an overview of the broad range of uses of ML in alloy research: in addition to work described here, ML has been applied to materials such as superconductors^{73–76} and phase-change memory materials⁷⁷, but an exhaustive discussion of every application is beyond the scope of this Review.

Metallic glasses

Metallic glasses are amorphous alloys in which the absence of crystalline order enables unexpected properties: the lack of slip planes results in high yield strength⁷⁸ and wear resistance, whereas corrosion resistance is enhanced by the absence of structural defects and grain boundaries slowing ion diffusion, making these materials potentially useful for biomedical implants⁷⁹. The identification of compositions with high glass-forming ability is a difficult task. Several different physical models have been proposed, based on atomic size difference and packing density^{80–83}, glass transition and melting temperature^{84–86}, and the competition between ordered phases^{87,88}. ML methods are being applied to identify new glass-forming compositions (TABLE 1).

Glass-forming ability. Glass formation in metal alloys has been investigated with a variety of ML approaches, including models based on RFs^{89–91}, support vector machines (SVMs)⁹², gradient-boosted decision trees⁹³, PCA⁹⁴, NNs^{95–99}, support vector regression and Gaussian process models¹⁰⁰, and linear regression¹⁰¹. Predicted properties related to glass-forming ability include reduced glass transition temperature^{94,96}, critical cooling rate⁹⁶, undercooled liquid region ΔT_x (difference between the glass transition temperature and the crystallization temperature)^{96,98,101}, critical casting diameter¹⁰⁰, crystallization temperature^{94,95} and liquidus temperature⁹⁴. Particularly important features include the difference between the actual liquidus temperature and that expected from a linear interpolation of the elemental melting temperatures⁹², the atomic radius difference⁹³, a large difference between the work function and heat of fusion, few valence electrons and a low boiling temperature¹⁰².

Machine reading using a classifier based on gradient-boosted trees was used to extract data from phase diagrams to find deep eutectics⁹³, known to be important for glass-forming ability. Eutectic points were characterized by the angle formed by the tangents of the liquidus lines — the narrower the angle, the deeper the eutectic — and by the difference between the liquidus temperature and the temperature obtained from the common tangent connecting the maximum temperature of the liquidus lines. A region of high glass-forming ability was found for compositions with a eutectic angle smaller than 75°, where the atomic radius of the majority species was slightly smaller than that of the minority species.

Alloy systems predicted to have a high glass-forming ability included Ag–Yb, Mg–Eu, Be–Fe, Ag–Te and Ag–Sm, with the composition range from Ag_{0.206}Yb_{0.794} to Ag_{0.326}Yb_{0.674} being particularly promising.

Out of 20 different ML methods applied to a glass formation data set with 6,471 alloy compositions¹⁰², RFs were found to give the best predictions by 100-fold cross-validation testing. The data set included the critical casting diameter for 5,934 compositions and 674 critical transformation temperature measurements. Key features for glass-forming ability were found to be large difference between the work function and heat of fusion, few valence electrons and a low boiling temperature. The glass transition, crystallization and liquidus temperatures were found to depend on the average melting temperature, and the liquidus temperature increased with decreasing average atomic radius.

Guiding experiments. ML models have been used to guide metallic glass synthesis^{89,90}, with the experimental results used to enhance the training set and retrain the models. RF-based models were developed⁸⁹ to investigate glass formation in combination with sputtering synthesis experiments⁹⁰. The original model was trained on a set of 5,369 experimentally characterized compositions¹⁰³, 70.8% of which were glass-forming, and showed good agreement with experiments for the Al–Ni–Zr system (FIG. 2a). The Co–V–Zr alloy system was synthesized using combinatorial magnetron co-sputtering to determine its glass-forming ability as a function of composition, and the new experimental data were used to retrain the model⁹⁰. Glass formation was observed in a region between Co₅₀Zr₅₀, Co₇₅Zr₂₅, V₅₀Zr₅₀ and V₇₅Zr₂₅. Results for original and retrained models for Co–Ti–Zr, Co–Fe–Zr and Fe–Ti–Nb are shown in FIG. 2b. The extra data were downsampled to 70 points so as not to bias the model based on one alloy system; this new data had the advantage of being better balanced with respect to the ratio of glass-forming to non-glass-forming compositions. The accuracy of the retrained model improved by a factor of 3 to 4. The model was later expanded to include additional glass formation attributes⁹¹, such as cluster packing efficiency and distance to crystalline compounds, as well as ΔT_x for 621 alloys.

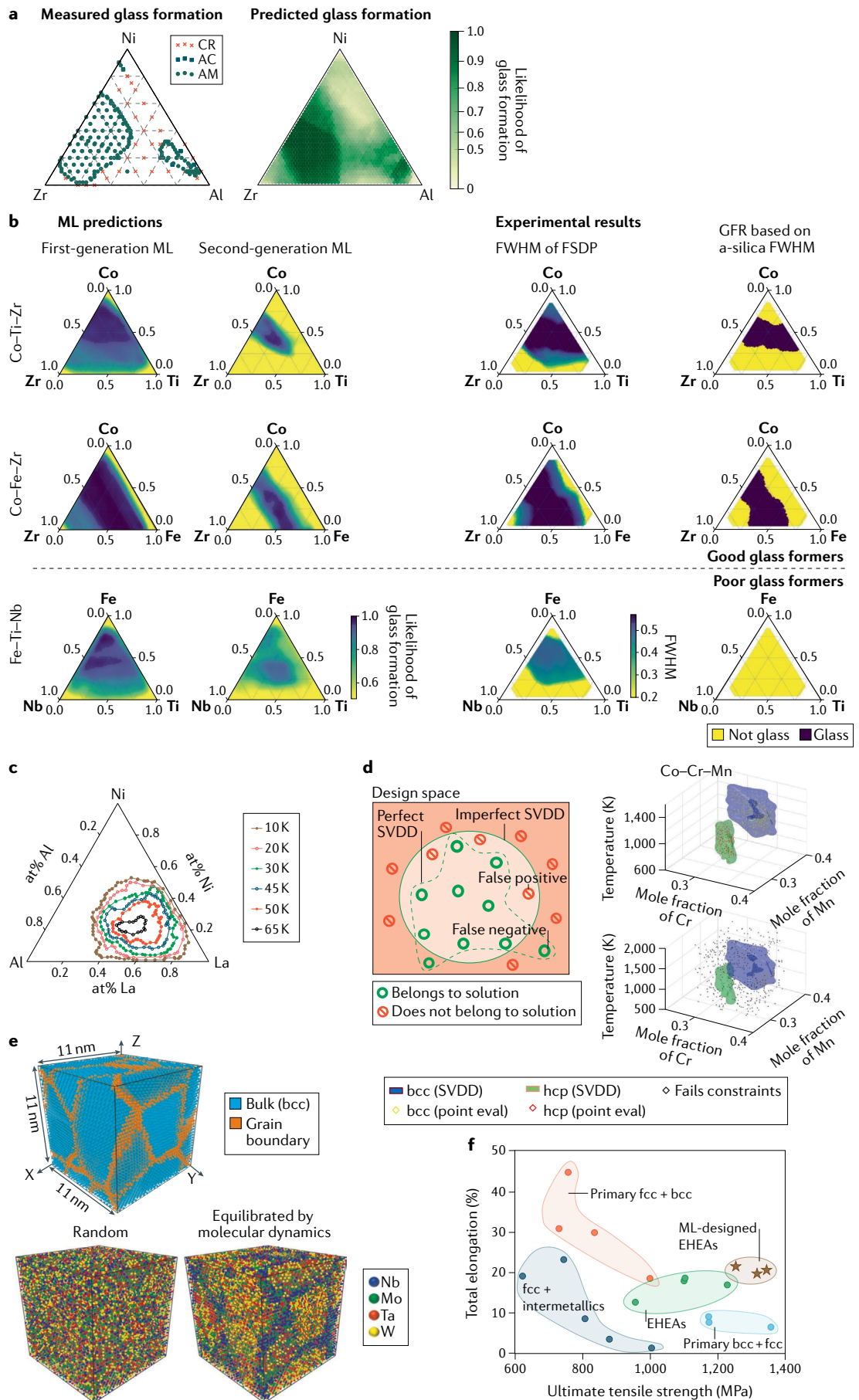
NNs were used to predict ΔT_x and guide the synthesis of Zr–Al–Ni–Cu glasses⁹⁸. A set of Zr–Al–Ni–Cu compositions was fabricated with arc-melting and ΔT_x was measured; the correlation between predictions and experiment was $R=0.9574$. The model was then used to predict ΔT_x for the Al–La–Ni system (FIG. 2c).

Elastic properties. Multiple models were trained to predict elastic properties of metallic glasses^{100,102}. Support vector regression gave a very good linear correlation with experimental results of up to 0.9799 and a leave-one-out cross-validation error of 8.2898 GPa when trained on a set of 219 elastic moduli¹⁰⁰. RFs trained on bulk and shear moduli for 278 bulk metallic glass compositions showed linear correlations of 0.9836 and 0.9843 (REF.¹⁰²); smaller atomic volumes gave larger bulk and shear moduli.

Table 1 | Overview of machine learning applications for disordered alloys

Year	Description	Refs
Metallic glasses		
2003	Linear regression for supercooled liquid region width for Mg-based alloys	101
2004	NNs to predict crystallization temperatures in Ni–P alloys	95
2007–2013	NNs to predict reduced glass transition temperature, critical cooling rate and undercooled liquid region of alloys, and to guide synthesis of Zr–Al–Ni–Cu glasses	96–99
2015	Principal component analysis on a set of 594 bulk metallic glass compositions	94
2016, 2018	RFs used to guide experimental synthesis of Co–V–Zr glasses	89–91
2017	SVM model trained on binary alloy data to predict glass-forming ability	92
2018	Delithiation in amorphous Li _x Si system modelled using a NN potential	267
2019	Classifier based on gradient-boosted tree to find deep eutectics in phase diagrams	93
2019	Support vector regression and Gaussian process models to predict elastic moduli and critical casting diameters of metallic glasses	100
2020	Twenty different ML models applied to glass formation data for 6,471 compositions; also predict elastic moduli	102
High-entropy alloys		
2008	NNs to investigate Hume–Rothery's rules for solid-solution formation	116
2014	NNs to predict structure formation (bcc, fcc or mixed phase) in high-entropy alloys	117
2015	Principal component analysis to identify underlying properties determining the formation of fcc or bcc solid solutions in TiMnFeNi, MnFeCoNi and TiVMnNb	123
2017	Approach based on multidimensional tensors to extend cluster expansion to include effects of relaxations from the ideal lattice in AgPt, AgPtAuPd and AgPtAuPdCuNiAl	131
2017	Gaussian process statistical analysis to predict solid-solution formation	119
2018	Constraint satisfaction algorithm combined with support vector domain descriptor to solve the continuous constraint problem to find desired stable phases	122
2018	NNs to predict formation of solid solution, intermetallic or amorphous phase	114
2018	Genetic algorithms, Gaussian process statistical analysis and CALPHAD used to design solid-solution hardened Al ₁₀ Co ₁₇ Fe ₃₄ Mo ₅ Ni ₃₄ high-entropy alloy	120
2018	Solid-solution hardened bcc Al–Cr–Mn–Mo–Ti alloys designed by a combination of genetic algorithms, CALPHAD, Pareto optimization and data mining	128
2019	Active learning machine-trained low-rank potential to run Monte Carlo simulations for MoNbTaW	134
2019	ML spectral neighbour analysis potential to investigate strengthening mechanisms in NbMoTaW	137
2019	k-Nearest neighbours, SVMs and artificial NNs to predict formation of solid solution, intermetallic or mixed solid solution and intermetallic phases	115
2019	NNs to find quasi-phase equilibrium for phase-field models for Al–Cu–Mg	118
2019	SVMs to predict phase formation in Co–Cr–Fe–Mn–Ni high-entropy alloys	121
2019	RFs to predict phase formation based on binary alloy phase diagram data	124
2019	MTPs to calculate vibrational energies of VNbMoTaW	132
2019	ML interatomic potential to investigate order–disorder transitions in FeNi and CoCrFeNi	135
2019	MTPs to investigate lattice distortion in CoFeNi	136
2019	Iterative feedback between ML and experiment to develop high-hardness Al–Co–Cr–Cu–Fe–Ni high-entropy alloys	138
2019	Gradient boosting trees combined with ab initio and experiment to investigate elastic properties of Al _{0.3} CoCrFeNi	139
2019	NNs to find the Al–Co–Cr–Fe–Mn–Ni composition with highest hardness	140
2019	Canonical correlation analysis combined with genetic algorithms to find hard high-entropy alloys; hardest alloy is Co ₃₃ W ₇ Al ₃₃ Nb ₂₄ Cr ₃ at 1084 HV(10.63 GPa)	141
2020	NNs to search for eutectics in Al–Co–Cr–Fe–Ni	142
2020	Logistic regression to predict phase formation in high-entropy alloys	125
2020	Genetic algorithms to find the best combination of descriptors and ML models to predict phase formation in high-entropy alloys	130
2020	Bayesian regression to handle underdetermined training data to develop a cluster expansion model to predict configuration energies of NbMoTaW, NbMoTaWV and NbMoTaWTi	133

bcc, body-centred cubic; CALPHAD, CALculation of PHAse Diagrams; fcc, face-centred cubic; ML, machine learning; MTP, moment tensor potential; NN, neural network; RF, random forest; SVM, support vector machine.



◀ Fig. 2 | Machine learning for disordered alloys. **a** | Comparison of machine learning (ML) predictions of glass formation with experimental results for Al–Ni–Zr. **b** | Comparison of first-generation and second-generation ML predictions with experiments for Co–Ti–Zr (top row), Co–Fe–Zr (middle row) and Fe–Ti–Nb (bottom row). The first column are the original ML predictions, the second column are predictions after retraining with new experimental data (active learning), the third column are experimental X-ray diffraction results and the fourth column shows a binary glass or non-glass result using a threshold based on amorphous silica (a-silica). Note how the agreement with the experimental data improves going from first-generation to second-generation ML. **c** | Predicted difference between glass transition temperature and crystallization temperature for Al–La–Ni. Large differences between the two temperatures, such as in the region encapsulated by the black circles, indicate thermal stability against crystallization when the glass is heated. **d** | Phase formation prediction for Co–Cr–Mn by support vector machines. The schematic on the right compares a perfect classification to an imperfect one. The plots on the left depict the bcc (blue) and hcp (green) phase regions for the Co–Cr–Mn system. The points that satisfy the constraints are shown in yellow and red on the top-right plot, and the points that do not satisfy them are shown in black on the bottom-right plot. **e** | Molecular dynamics simulation with spectral neighbour analysis potential for Nb–Mo–Ta–W, showing Nb segregating to the grain boundaries, while W is enriched in the bulk (bcc). **f** | Ashby plot for total elongation against ultimate tensile strength for eutectic Al–Co–Cr–Fe–Ni alloys, which overcome the strength–ductility trade-off. AC, partially amorphous ribbon formation; AM, fully amorphous ribbon; bcc, body-centred cubic; CR, compositions with no appreciable formation of amorphous phase; EHEA, eutectic high-entropy alloy; fcc: face-centred cubic; FSDP, first sharp diffraction peak; FWHM, full width at half maximum; GFR, glass-forming region; SVDD, support vector domain description. Panel **a** reprinted from REF.⁸⁹, CC BY 4.0 (<https://creativecommons.org/licenses/by/4.0/>); panel **b** reprinted with permission of AAAS from REF.⁹⁰, © The Authors, some rights reserved; exclusive licensee AAAS. Distributed under a CC BY-NC 4.0 License (<http://creativecommons.org/licenses/by-nc/4.0/>); panel **c** adapted with permission from REF.⁹⁸, Elsevier; panel **d** reprinted with permission from REF.¹²², Elsevier; panel **e** reprinted from REF.¹³⁷, CC BY 4.0 (<https://creativecommons.org/licenses/by/4.0/>); and panel **f** adapted with permission from REF.¹⁴², Elsevier.

High-entropy alloys

High-entropy alloys typically have at least four principle elements and can form single-phase solid solutions^{104–110}. This atomic structure gives them unique properties that have applications in a variety of technologies. For example, high-entropy alloys demonstrate improved fracture resistance at cryogenic temperatures¹¹¹, and the formation of ordered precipitates can be engineered to optimize mechanical properties such as the strength–ductility ratio^{109,112,113}. The complexity of these materials poses a challenge for computational researchers, providing promising opportunities for the application of ML (TABLE 1).

Phase formation. Phase (for example, solid solution) formation in high-entropy alloys has been investigated using NNs^{114–118}, Gaussian process statistical analysis^{119,120}, *k*-nearest neighbours¹¹⁵, SVMs^{115,121,122} (FIG. 2d), PCA¹²³, RFs¹²⁴ and logistic regression¹²⁵. These studies revealed that valence electron concentration^{114,115,123,125}, electronegativity^{114,116}, atomic radius^{115,116} and mixing enthalpy¹²³ are all important features in determining phase formation. By contrast, the mixing entropy, as obtained from the ideal configuration entropy $S = \sum_i x_i \log x_i$, was found to be relatively insignificant^{114,115,125}, possibly due to ordering effects at finite temperature reducing the actual entropy of the material^{114,126,127}. A structural parameter based on the crystal system and the unit cell size and shape was also found to not be important¹¹⁶, and even counter-productive for low-solubility/low-concentration systems. Valence electron concentration was found to determine

the atomic stacking character (fcc or bcc)^{117,128}. In general, a major limitation to this approach is the accuracy of the input data: the atomic radius, in particular, is not always well defined¹¹⁶. RFs were used to predict the formation of single-phase high-entropy carbides¹²⁹. The models were trained on spectral descriptors for high-entropy materials obtained with ab initio calculations³⁸. Several new Cr-containing compositions were predicted; experimental synthesis by arc melting and characterization by X-ray diffraction confirmed single-phase formation.

Genetic algorithms were used to determine which combinations of features and ML models were most effective in predicting phase formation¹³⁰. A total of 70 descriptors were investigated and model improvement was found to saturate for ~4 descriptors. SVMs with a radial basis kernel performed best at classifying solid solution formation or non-formation, whereas the NN approach performed best at classifying the type of solid solution formed. The genetic algorithm approach outperformed other methods for reducing the feature space, such as LASSO, RFs, sequential forward selection and gradient tree boosting. 12,647 compositions forming high-entropy alloys were predicted: 845 based on an fcc lattice, 9,302 based on bcc and 2,500 with dual bcc/fcc phase structure. Ten compositions with high classification uncertainty were chosen for synthesis: eight were found to be forming non-solid solutions, one formed a bcc phase and one a dual bcc/fcc phase. The classifiers were retrained using the new data (active learning), improving classification accuracy.

Configuration energies. Machine-learned models have been used to predict energies for different atomic configurations^{131–133}, as an extension or alternative to using cluster expansions. A new way to construct lattice models based on a low-rank ‘tensor train’ representation was shown to be particularly effective for alloys with a large number of components¹³¹. The interatomic potential was trained and validated on ab initio calculations for 32-atom cubic cells on the fcc lattice. Validation accuracies of 3 meV per atom were achieved for the AgPt, AgPtAuPd and AgPtAuPdCuNiAl alloy systems. The error depended on the number of different columns in the periodic table that the elements came from, because replacing an element with one with the same number of valence electrons created a more local perturbation, making it easier to fit by a short-range interatomic potential. The model was fitted to predict the formation energies of alloys with up to 23 elements on a training set of 1,600 configurations and showed significantly lower errors than for a cluster expansion containing nearest-neighbour pairs and triples trained using compressive sensing.

Thermo-mechanical properties. Machine-learned interatomic potentials have been used to study the thermodynamic^{132,134,135} and mechanical properties^{136,137} of high-entropy alloys. A machine-learned low-rank potential, trained using active learning on ab initio calculations for 200 randomly generated configurations, was used to run Monte Carlo simulations for the MoNbTaW alloy¹³⁴. The vibrational contribution to the formation

energy was found to be negligible (<0.1 meV per atom) and phase transitions were observed to the B2 structure (Mo,W,Nb,Ta) at ~600 K and then to B2 (Mo,Ta) and B32 (Nb;W) at ~600 K. The model's energy predictions agreed well with ab initio calculations for the ground, semiordered and disordered states, deviating by 0.1, 1.7 and 0.4 meV per atom, respectively.

Machine-learned interatomic moment tensor potentials, which describe the atomic environments with moment tensor descriptors, were used to investigate lattice distortion in the ternary alloy CoFeNi (REF.¹³⁶). Heating and quenching produced a mixture of static and dynamic distortions that reduced the elastic moduli. No short-range order correlations were found for Co and Ni, but some ordering was found for Fe–Fe and Ni–Fe atom pairs. The asymmetry of moment tensor potentials enabled them to capture anharmonic contributions to the vibrational energy of VNbMoTaW (REF.¹³²).

A machine-learned ‘spectral neighbour analysis potential’ was used to investigate the strengthening mechanisms in NbMoTaW (REF.¹³⁷). The potential was trained on DFT calculations of a combination of special quasi-random, ground state and molecular dynamics structures. After equilibration, Nb segregates to the grain boundaries, whereas W is enriched in the bulk (FIG. 2e). The equilibrated alloy has higher strength than the random alloy, similar to that of W, the strongest element, owing to the Nb enrichment at the grain boundaries reducing the von Mises strain.

ML models and data mining have been combined with experiment to investigate the mechanical properties, and, in particular, to optimize the hardness, of high-entropy alloys^{128,138–140}. An iterative feedback procedure between ML predictions and experiments was used to develop high-hardness high-entropy alloys in the Al–Co–Cr–Cu–Fe–Ni family¹³⁸. The lowest root-mean-square errors were found for support vector regression with a radial kernel, back-propagation NNs and *k*-nearest neighbours. After iterating between ML and experiment, the composition Al₄₅Co₂₄Cr₂₂Fe₅Ni₆ was found, with Vickers hardness of 865 HV (8.48 GPa). Introducing materials descriptors, along with mechanical properties such as shear modulus and lattice distortion energy, reduced the cross-validation error to 54.4 HV (0.53 GPa). The highest-hardness composition was Al₄₇Co₂₀Cr₁₅Cu₅Fe₅Ni₅, with 883 HV (8.66 GPa), which formed a bcc solid solution with a NiAl B2 ordered phase.

A gradient boosting trees approach using weak learners was combined with ab initio calculations and experimental measurements to investigate the elastic properties of Al_{0.3}CoCrFeNi (REF.¹³⁹). Shapley additive explanations showed that the bulk modulus depends on the electronegativity of the most electronegative element, whereas the shear modulus depends on the least electronegative element. The high-entropy alloy was observed to have a wide spread of interatomic distances even between atoms of the same type. In particular, Cr–Cr distances varied based on the other neighbouring atoms, owing to magnetic interactions, demonstrating that magnetic frustration can drive lattice distortion in these systems.

A NN was trained to find the composition with the highest hardness in the AlCoCrFeMnNi high-entropy

alloy system¹⁴⁰. The training set consisted of 91 hardness measurements for binary to hexenary compositions, prepared with vacuum arc melting. Simulated annealing was used to find the optimum composition of Al₂₄Co₁₈Cr₃₅Fe₁₀Mn_{7.5}Ni_{5.5} with a predicted hardness of 670 ± 98 HV (6.57 ± 0.96 GPa) and a measured hardness of 650 ± 12 HV (6.37 ± 0.12 GPa), exceeding the highest value in the literature for this system of 539 HV (5.29 GPa). The high hardness is due to bcc/B2 precipitates forming, owing to high Al content. Solid-solution hardened bcc alloys were designed by a combination of genetic algorithms, CALPHAD (CALculation of PHase Diagrams), Pareto optimization and data mining¹²⁸.

Compositions formed from a set of 16 elements were generated with elemental concentrations varying from 5 at% to 35 at% in steps of 1 at%. 3,155 Pareto-optimal alloys were found, and experimental synthesis and characterization of a selected composition indicated a Vickers hardness of 6.45 GPa (658 HV), one of the hardest reported for a metal alloy with such a low density.

Canonical correlation analysis was combined with genetic algorithms to design hard high-entropy alloys¹⁴¹. Input data consisted of the Vickers hardness for 82 systems. Multiple regression was performed with canonical correlation analysis to predict the presence of bcc or fcc solid solutions or of intermetallic phases, and to predict the Vickers hardness. Hardness was found to increase with ideal mixing entropy and decrease with valence electron concentration and mixing enthalpy. Canonical correlation analysis was used to construct a fitness function for a genetic algorithm search in a composition space of 16 metallic elements. Seven of the predicted alloys were synthesized: hardnesses ranged from 277 HV (2.72 GPa) to 1,084 HV (10.63 GPa); five of the alloys had hardness greater than 700 HV (6.87 GPa).

Identifying eutectics. An artificial NN was used to search for eutectics in the Al–Co–Cr–Fe–Ni high-entropy alloy system¹⁴². It was found that eutectic points were most common for compositions with Cr concentration lower than 25% and Al concentration between 15% and 20%, whereas the distribution was similar across concentrations of the other three elements. Increasing the Ni concentration resulted in fcc formation, whereas more Fe resulted in bcc formation, owing to changes in the valence electron concentration. The resulting eutectic alloys had improved mechanical properties; in particular, they overcame the strength–ductility trade-off (FIG. 2f).

Catalysts. The IrPdPtRhRu high-entropy alloy was used as a discovery platform for catalysts for the oxygen reduction reaction¹⁴³. Sequential least-squares programming was used to find compositions giving optimal adsorption energies, according to the Sabatier model for catalytic activity. The optimum five-component composition was found to be Ir_{10.2}Pd₃₂Pt_{9.3}Rh_{19.6}Ru_{29.8}, whereas relaxing the restriction on the number of elements gave the optimum composition of Ir_{17.5}Pt_{82.5}, with a predicted activity 28 times higher than Pt. Adjusting the adsorption energies to account for strain gave an optimum composition of Ir_{59.1}Pt_{40.9}.

Shape-memory alloys

Shape-memory alloys are systems that undergo simultaneous size and shape changes during a phase transformation. Their applications include sensors, actuators and biomedical implants, such as stents. Relevant properties include the transformation temperature, shape-memory recovery ratio, superelasticity and hysteresis due to differences in the heating and cooling transformation temperatures, which can lead to fatigue. ML has been incorporated into experimental design to find alloys with low thermal hysteresis¹⁴⁴, to simultaneously optimize thermal hysteresis and transition temperatures¹⁴⁵, and to develop precipitation-strengthened NiTi shape-memory alloys¹⁴⁶. Models have also been constructed to predict transition temperatures^{62,147} and to investigate laser powder-bed fusion fabrication¹⁴⁸. An overview of ML works on shape-memory alloys is provided in TABLE 2.

ML and adaptive design have been used to investigate and optimize shape-memory behaviour in the $Ti_{50}Ni_{50-x-y-z}Cu_xFe_yPd_z$ alloy system^{144,145,147} (FIG. 3a). This system undergoes cubic to rhombohedral (B2 to R) or cubic to orthorhombic monoclinic (B19, B19') phase transitions. To find compositions with minimum thermal hysteresis (ΔT), Gaussian process models and support vector regression with linear and radial basis function kernels were fitted to data obtained by synthesizing and characterizing 22 compositions¹⁴⁴. Efficient global optimization, knowledge gradient and pure exploitation ‘min’ algorithms were used to propose new compositions. A combination of support vector regression with radial basis functions and knowledge gradient was found to work best, finding a new alloy, $Ni_{46.7}Ti_{50}Cu_{0.8}Fe_{2.3}Pd_{0.2}$, with $\Delta T = 1.84$ K. Ab initio calculations were performed to check the energetics of transformations, indicating that the low ΔT for this composition was due to a low activation barrier and small energy difference between the phases. Models were also constructed for the transition temperatures of this system using linear and polynomial regression, and support vector regression¹⁴⁷. Polynomial regression (linear in valence electron number and Pauling electronegativity, and quadratic in Waber–Cromer’s pseudopotential radii) gave a good mix of accuracy and interpretability, and worked well for 23 other test systems from the literature. The model was used in combination with efficient global optimization, knowledge gradient and maximum exploitation algorithms to find the composition with the highest transition temperature. The best candidate was $Ti_{50}Ni_{25}Pd_{25}$, with a predicted transition temperature of 189.56 °C and a measured value of 182.89 °C. The Pareto front (FIG. 3b) for transition temperatures versus thermal hysteresis was investigated for this system, to minimize both properties simultaneously¹⁴⁵. Gaussian process regression and support vector regression with a radial basis function kernel were fitted to experimental data. Maximin and centroid exploration algorithms were more effective than random, pure exploitation or pure exploration approaches at finding the Pareto front in as few cycles as possible.

A 2D time-dependent Ginzburg–Landau model for the austenite to martensite phase transition and elasticity was developed for alloy systems such as FePd and InTl (REF.¹⁴⁹). The model describes the free energy as a

function of stress and strain, whereas the dilatational stresses due to dopants are modelled by Gaussian distributions centred on the impurity. The model was used to search for materials with low energy dissipation, modelled as a function of dopant potency, distribution and concentration.

Bayesian optimal experimental design was applied to Ni_4Ti_3 precipitation-strengthened NiTi shape-memory alloys¹⁴⁶. Stress–strain equations were solved using finite element modelling, using elastic constants of B2 austenitic and Ni_4Ti_3 rhombohedral structures obtained from first-principles calculations, and the results were used to train a Gaussian process regression surrogate model. Selection of test compositions was based on expected hypervolume improvement and pure exploitation. The method was used to search for an alloy with an austenitic finish temperature of 30 °C and a specific hysteresis temperature of 40 °C. No composition was found satisfying these criteria, so the Pareto front was generated to find the compositions closest to the target. The search efficiency was optimized by using the algorithm from the very start to choose the initial training data points, instead of initializing with multiple randomly chosen points.

Laser powder-bed fusion was investigated for the additive manufacturing of shape-memory alloys¹⁴⁸. NiTi is difficult to machine and very sensitive to composition: small variations in Ni content can change the transformation temperature by 100 °C. Fabrication success using laser fusion of powder was evaluated as a function of linear, surface and volume power density, which are functions of laser power, scan speed and hatch spacing. Linear discriminant analysis revealed that high values of linear power density led to high printability, whereas hatch spacing made little difference. Linear power density had little effect on transition temperatures, but the volume power density did have an effect. Hatch spacing affected microstructure and transition temperature, but not printability.

Support vector regression, RFs and Gaussian process regression were trained to predict the transition temperatures and hysteresis of NiTiHf shape-memory alloys as a function of composition and heat treatment processing⁶². Owing to the nature of the dependence of the phase transformation rate on the processing conditions, the models were more accurate when the heat treatment time and temperature were represented by logarithmic and sigmoid functions. The models worked reasonably well for transition temperatures but were unreliable for predicting hysteresis values.

Superalloys

Ni single-crystal superalloys display high creep resistance due to precipitation of the $L1_2$ γ' intermetallic phase in the austenitic fcc γ solid-solution matrix with coherent {100} interfaces¹⁵⁰. ML has been used to design new alloy compositions with optimized properties^{151–154} and to model the lattice misfits^{150,155} and interfaces¹⁵⁶ of the γ and γ' phases (TABLE 2).

Superalloy design. Gaussian processes were combined with CALPHAD and genetic algorithms to design Ni-based superalloys^{151,152}. Thermodynamic phase

Table 2 | Overview of machine-learning applications for shape-memory alloys, superalloys, catalysts and magnets

Year	Description	Refs
Shape-memory alloys		
2016–2018	ML and adaptive design to optimize thermal hysteresis and transition temperatures in the $T_{50}Ni_{50-x-y-z}Cu_xFe_yPd_z$ alloy system	144,145,147
2017	2D time-dependent Ginzburg–Landau model for austenite to martensite phase transition and elasticity in alloy systems such as FePd and InTl	149
2018	Bayesian optimal experimental design for Ni_4Ti_3 precipitation-strengthened NiTi shape-memory alloys	146
2018	Linear discriminant analysis to optimize laser powder-bed fusion for additive manufacturing of NiTi alloys	148
2021	Support vector regression, RFs and Gaussian process regression to predict composition–process–property relationship for NiTiHf alloys	62
Superalloys		
1998	NNs to model lattice parameters for γ and γ' phases as function of composition and temperature	155
2013, 2016	Gaussian processes combined with CALPHAD and genetic algorithms to design Ni-based superalloys	151,152
2017	NNs combined with CALPHAD to find Ni-based compositions optimizing fatigue life, yield stress, tensile strength, γ' fraction and Cr activity	153
2018	ML models to predict the misfit between the γ and γ' phases	150
2018	NNs combined with genetic algorithms to design Ni-based superalloys for ultra-critical steam plants	154
2019	ML models to predict the energy of different configurations to model γ – γ' interfaces	156
Catalysis and alloys		
2012–2019	Cluster expansions to predict the structures and properties of alloy nanocatalysts	179–185
2014, 2015	NN potentials to identify structures and properties of Au–Cu alloy nanocatalysts	187,188
2015, 2017	NNs to predict adsorption energies on alloys as a function of physical properties of the surface and the local environment of the adsorption site	166–168
2015, 2019	Bayesian cluster expansions to predict equilibrium surface structures and catalytic activities of bulk Pt–Ni alloys	177,178
2017	‘Bootstrapped projected gradient descent’ to identify relevant descriptors for CO binding energies on alloy surfaces	169
2017	NNs to predict surface segregation in the Au–Pd alloys	175
2017	SOAP descriptors to predict the structures and activities of Rh–Au nanoparticles	191
2018	Multiple types of regression evaluated for predicting adsorption energies on embedded single-atom catalysts	170
2018	NN potential to study atomic order in icosahedral Cu–Ni–Pt nanoparticles	189
2018	SOAP descriptor to predict hydrogen adsorption energies on small Au–Cu clusters	192
2018, 2020	ML to predict adsorption energies based on the local environment of the adsorption site to guide discovery of new catalysts for CO_2 reduction and hydrogen evolution	172,174
2019	Lattice pair potential to calculate adsorption energies and optimize the composition of a high-entropy alloy for catalysing oxygen reduction	143
2019	Graph NNs to predict adsorption energies on a variety of surfaces	173
2019	SISSO algorithm to identify descriptors for binding energies for representative adsorbates on alloy surfaces	171
2019	NN potentials to accelerate searches for low-energy structures for small bimetallic and trimetallic clusters	190
Magnetism and alloys		
2014	On-the-fly ML to analyse XRD data for Fe–Co–X (X = Mo, W, Ta, Zr, Hf, V) films to find phases with strong magnetic anisotropy	195
2017	NNs to extract order parameters corresponding to phase transitions from Monte Carlo configuration data for ferromagnetic Ising model	193
2017	NNs to find topological phase transitions in the Kitaev chain, phase transitions in the Ising model and many-body localization transitions in disordered quantum spin chains	194
2018	CALPHAD and k-nearest neighbours to find processing–structure–property linkages in soft magnetic alloys, such as FINEMET alloys forming Fe_3Si precipitates	196
2019	RFs, NNs, ridge regression and kernel ridge regression to predict the Curie temperature	197

CALPHAD, CALculation of PHase Diagrams; ML, machine learning; NN, neural network; RF, random forest; SISSO, sure independence screening and sparsifying operator; SOAP, smooth overlap of atomic positions; XRD, X-ray diffraction.

stability was predicted using the Thermo-Calc software with the TTNi database. Acceptable microstructures were restricted to those containing only γ , γ' and $M_{23}C_6$ phases, avoiding Laves and other deleterious phases. Gaussian process regression was trained on experimental data to predict ultimate tensile stress, yield stress, creep rupture stress, and the γ and γ' lattice parameters. Input features included composition and processing history (forging, cold deformation and treatment temperature) and the output was creep rupture stress. The optimal alloy minimizing the creep rupture stress per unit cost had a γ' content of 24.8% at 750 °C: low enough to be easily weldable and avoid strain-age cracking¹⁵¹. To find an alloy realistic for high-temperature structural applications, the ultimate tensile strength, yield stress and creep rupture stress were maximized, while the γ - γ' misfit parameter and brittle temperature range were minimized¹⁵². 5,669 alloys were predicted on the Pareto front. A slightly cheaper and more weldable alternative to Inconel 740H (In740H) and Haynes 282 was proposed, where more γ' phase due to increased Al content offset the loss of strength due to lack of Nb. An alternative to Alloy 263 was proposed that avoided the formation of η platelets due to lower Ti content.

NNs and CALPHAD were used to find Ni-based superalloy compositions that optimize fatigue life, yield stress, tensile strength, γ' fraction and Cr activity (for corrosion resistance)¹⁵³. The models were trained on experimental data for properties as a function of composition and heat treatment, and were combined with an optimizer incorporating error estimates (Bayesian bootstrap approach) to search for an alloy with a yield strength exceeding 752 MPa at high temperatures. Experimental verification was performed on the optimal alloy: the γ' fractional volume was 51% and the yield stress was 765 MPa.

NNs and genetic algorithms were combined to design Ni-based superalloys for ultra-critical steam plants that improved on In740H (REF.¹⁵⁴). Training data were extracted from the literature for 580 instances: model inputs included the concentrations of 14 elements, and γ and γ' contents; outputs included the γ - γ' mismatch, yield stress and creep rupture life. Experimental validation indicated that the new alloy had a yield strength of 597 MPa at 750 °C and a creep life exceeding 3,691 h (with a prediction of 5,800 h at 150 MPa), extrapolated to 9,100 h at 135 MPa, compared with In740H, which has a yield strength of about 580 MPa at 750 °C and a creep life of about 10,000 h at 150 MPa stress.

γ and γ' phase properties. NNs were used to model the lattice parameters for the γ and γ' phases as a function of composition and temperature already in 1998 (REF.¹⁵⁵). The lattice mismatch between the γ and γ' phases in Ni superalloys controls the coarsening behaviour and the dislocation glide at the γ - γ' interface. Composition and temperature were used as input for the model, and the lattice constants were the output. Al was found to be most important for the lattice constant of the γ phase and Ti most important for the γ' phase. Lattice constants for γ were sensitive to Mo content and for γ' to Nb content. The lattice constant of the γ phase was generally

more sensitive than that of the γ' phase to composition changes.

ML models including support vector regression, sequential minimal optimization regression and multi-layer perceptron were used to predict the misfit between the γ and γ' phases¹⁵⁰. The training set consisted of data for 136 alloys extracted from the literature, with features including composition, dendrite positions, specimen thickness and temperature. Multilayer perceptron had the lowest mean average error and root-mean-square error. The model was validated against experimentally measured misfits, where it outperformed empirical models from the literature.

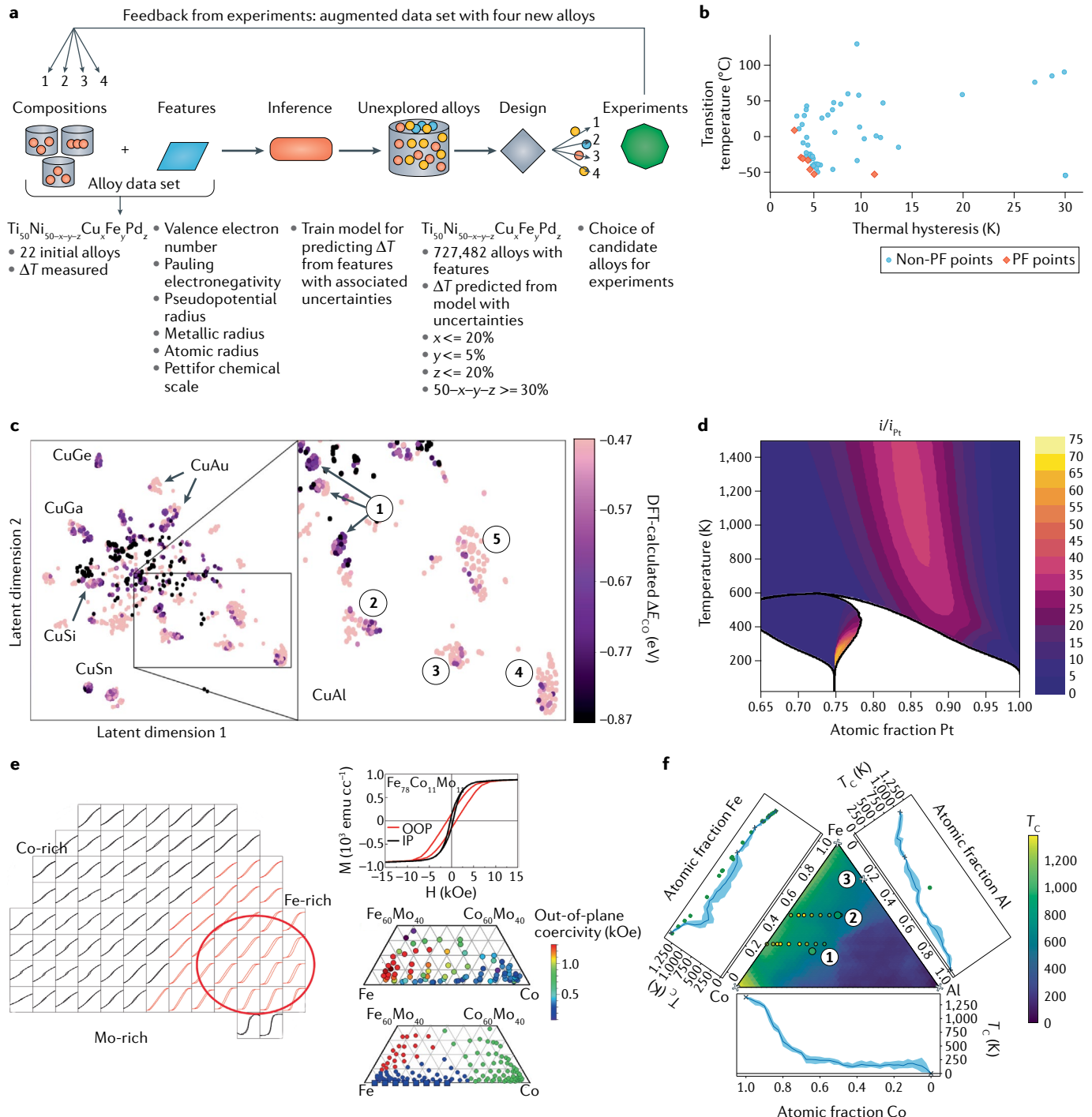
The γ - γ' interface in the Ni 617 superalloy was investigated using linear regression, ridge regression, kernel ridge regression, LASSO, support vector regression and Bayesian ridge regression to predict the energy of different configurations¹⁵⁶. All methods outperformed cluster expansion, with kernel ridge regression giving the lowest errors¹⁵⁶.

Catalysis and alloys

ML is increasingly being used to discover or design new catalysts (TABLE 2). Here, we focus on alloy catalysts. For a more general discussion of the use of ML in catalysis, we refer the reader to other reviews^{157–160}.

Computational searches have long made use of simple descriptors to predict catalytic activity without the need to explicitly model all steps of the chemical reaction. Adsorbate binding energies are particularly effective descriptors, as they can be used to estimate the activation energy through the Brønsted–Evans–Polanyi principle^{161,162}. This is a perfect scenario for ML deployment. For example, a model equivalent to a pairwise cluster expansion was constructed to predict adsorption energies for O and OH on different sites in IrPdPtRhRu high-entropy alloys, with an estimated prediction error of less than 0.1 eV (REF.¹⁴³). However, material-specific surrogate models are generally not well suited for high-throughput screening, owing to the computational expense of enforcing compatibility with each of the candidate materials.

An alternative approach, generally less accurate but more amenable to high-throughput screening, is to predict adsorption energies based on the physical descriptors of the bare surface. For example, physical and chemical reasoning was used to identify the surface electronic *d*-band centre as a descriptor of adsorption energies^{163,164}. ML can extend the formalism by identifying additional descriptors and more complicated models for adsorption energies^{70,165–173}. Some of the early work focused on developing NN models to predict adsorption energies as a function of properties of the surface and the atoms near the adsorption site^{166–168}. These models were used to screen alloy surfaces for CO₂ reduction¹⁶⁸ and methanol electro-oxidation¹⁶⁷. Similarly, ML models were developed for predicting adsorbate binding energies based on the properties of the adsorption site (such as the coordination number) and neighbouring elements (such as Pauling electronegativities)¹⁷². These models were used to guide high-throughput ab initio calculations of adsorbate binding energies on ideal



intermetallic surfaces, leading to 100 promising catalysts for CO_2 reduction or hydrogen evolution. Following these predictions, Cu–Al alloy catalysts have recently been developed that reduce CO_2 to ethylene with very high selectivity¹⁷⁴ (FIG. 3c). Finally, adsorption energies on a variety of surfaces can be predicted using graph NNs, in which the nodes of the network are mapped to atoms and the edges are mapped to connections between neighbouring atoms¹⁷³.

Models that relate physical descriptors to adsorbate binding energies can also be used to identify the most relevant descriptors. For example, the relative importance

of different physical descriptors was determined through sensitivity analysis of the developed NN models^{167,168}, and bootstrapped projected gradient descent¹⁶⁹ was used to identify relevant descriptors for CO binding energies on some of the same alloys^{167,168}. It was found that, in addition to characteristics of the electronic d -band, the work function is also a relevant descriptor¹⁶⁹. Subsequent work using multiple regression trees to predict the CH_3 adsorption energy on single-atom catalysts embedded in Cu surfaces found that the group and the surface energy of the doped element are the most predictive descriptors out of a dozen evaluated¹⁷⁰. Later on,

Fig. 3 | Machine learning for shape-memory alloys, catalysts and magnets. **a** | Adaptive design workflow for the optimization of the shape-memory alloy $Ti_{50}Ni_{50-x-y-z}Cu_xFe_yPd_z$. **b** | Pareto front (PF) for optimal combination of thermal hysteresis and transition temperature for shape-memory alloys generated using adaptive design. **c** | t-Distributed stochastic neighbour embedding (t-SNE) representation of how the CO adsorption energy varies among adsorption sites on Cu alloys based on local environment and composition. Sites that are close to each other tend to have similar features. Labels 1–5 indicate different types of sites for Al–Cu alloys: Al-heavy Cu sites, Cu-heavy Cu–Cu sites, balanced Al–Cu sites, Al-heavy Al–Al sites and Al-heavy Al sites, respectively. **d** | The current density (i) of (111) surfaces of Pt–Ni alloys in the Pt-rich region of the phase diagram, relative to that of Pt(111) (i_{Pt}), as predicted using a Bayesian cluster expansion. **e** | Magnetic and coercive field maps and structural property maps for a Co–Fe–Mo system generated by experiments guided by on-the-fly machine learning. Out-of-plane (OOP) hysteresis loops are shown for different compositions (left), along with typical OOP and in-plane (IP) hysteresis loops (top right). The coercive field map as a function of composition is shown on the centre right and the clustering results on the bottom right. Clustering techniques were used to group structurally similar regions together, with similar compositions shown by same-coloured dots in the bottom-right plot. **f** | Predicted Curie temperatures, T_C , for Al–Co–Fe. Crosses and circles indicate experimental data included and not included in the training set, respectively; numbers 1, 2 and 3 correspond to the known stoichiometric phases Co_2FeAl , Fe_2CoAl and Fe_3Al . ΔE_{CO} , DFT-calculated change in energy upon CO adsorption; ΔT , thermal hysteresis; DFT, density functional theory. Panel **a** adapted from REF.¹⁴⁴, CC BY 4.0 (<https://creativecommons.org/licenses/by/4.0/>); panel **b** adapted from REF.¹⁴⁵, CC BY 4.0 (<https://creativecommons.org/licenses/by/4.0/>); panel **c** reprinted from REF.¹⁷⁴, Springer Nature Limited; panel **d** adapted with permission from REF.¹⁷⁸, PNAS; panel **e** reprinted from REF.¹⁹⁵, Springer Nature Limited; and panel **f** reprinted with permission from REF.¹⁹⁷, APS.

the SISSO algorithm⁷⁰ was used to obtain descriptors for binding energies for six different representative adsorbates¹⁷¹. Using this approach, the d -band centre was rediscovered as the best simple descriptor, and more complex descriptors that had significantly lower errors on the alloy surfaces in the validation set were identified.

A great challenge in developing alloy catalysts is that adsorbate binding energies (and, hence, catalytic activity) can be highly sensitive to the atomic structure of the surface, often quite different from that of the underlying bulk material. Some degree of surface segregation is common in substitutional alloys (the concentration of one species is higher near the surface than in the bulk). Likewise, atomic order near the surface can be significantly different than in the bulk: an ordered intermetallic phase may have increasing disorder near the surface or a disordered solid solution may be covered by a monolayer skin consisting nearly entirely of a single element. Predicting the atomic structure of alloys' surfaces can be accomplished with ML energy models^{175,176}. When combined with descriptors of catalytic activity, this approach helps rational design of new catalysts. Bayesian cluster expansion and Sabatier volcano plots were used to predict the activities for the oxygen reduction reaction on (111) surfaces of ordered Pt_3Ni (REF.¹⁷⁷). The work was extended to Pt–Ni alloys in the entire Pt-rich portion of the temperature–composition phase diagram¹⁷⁸ (FIG. 3d). It was found that slightly Pt-rich Pt_3Ni should have the maximum activity, in good agreement with experimental results.

Alloy nanoparticles are of particular interest, owing to their high surface-to-volume ratios and the ability to adjust the catalytic properties by tuning particle shape. The size and complexity of these catalysts limits the extent to which ab initio methods can be used to directly model them, but this problem can be overcome through

the use of ML surrogate models. For example, cluster expansion has been used to predict equilibrium^{177,179–181} and non-equilibrium alloy nanoparticle structures^{182,183}, surface d -band centres¹⁷⁹ and adsorbate binding energies^{180,184,185}. Behler–Parrinello NN potentials were used¹⁸⁶ to identify equilibrium structures of Au–Cu alloy nanoparticles in vacuum¹⁸⁷ and aqueous environments¹⁸⁸. Coupling these potentials with ab initio calculations of adsorbate binding energies on small nanoparticles provided insights into solvation's effects on nanoparticle activity. NN potentials were similarly used to study surface segregation in icosahedral Cu–Ni–Pt nanoparticles and to identify design guidelines for oxygen reduction catalysts¹⁸⁹. NN potentials have also been used to accelerate searches for low-energy structures for small bimetallic and trimetallic clusters¹⁹⁰. Gaussian approximation potentials⁹ with the SOAP descriptor⁸ were used to model adsorption of N, O and NO on Rh–Au alloy surfaces¹⁹¹. This method could predict turnover frequencies for NO decomposition at different surface sites on cubooctahedral Rh–Au nanoparticles of varying size, composition and atomic order. The SOAP descriptor was generally found to perform at least as well as other leading descriptors in predicting hydrogen adsorption energies on small Au–Cu clusters¹⁹².

Magnetism and alloys

ML has been used to model magnetic properties, with applications ranging from investigating phase transitions in Ising-type models^{193,194} to analysing experimental phase diagrams of specific magnetic alloys¹⁹⁵, as well as modelling processing–structure–property linkages¹⁹⁶ and predicting Curie temperatures, T_C (REF.¹⁹⁷) (TABLE 2).

NNs were used to extract order parameters corresponding to phase transitions (such as T_c/J) from raw Monte Carlo configuration data for a ferromagnetic square-lattice Ising model, $H = -J \sum_{ij} \sigma_i^z \sigma_j^z$ (REF.¹⁹³). The models were also applied to the 2D square ice Hamiltonian and the Ising lattice gauge theory. The ordinary NNs had an accuracy of only 50% for the latter system, so a convolutional NN was used instead, which had accuracy of 100% at $T=0$ and $T=\infty$, with $T^*/J = 1/\log_e \sqrt{N}$, where T^* is the crossing temperature and N is the number of spins in the system.

NNs were used to find topological phase transitions in the Kitaev chain, phase transitions in the Ising model and the many-body localization transition in a disordered quantum spin chain¹⁹⁴. Supervised and unsupervised methods were combined, by bootstrapping the supervised model to unsupervised groups, finding patterns in the data and letting the user decide if changes corresponded to phase transitions. The method was successfully applied to the Ising model and the many-body localization transition: $H = J \sum_{i=1}^L S_i \cdot S_{i+1} + \sum_{\alpha=x,y,z} \sum_{i=1}^L h_i^\alpha S_i^\alpha$.

CALPHAD was combined with k -nearest neighbours models to find processing–structure–property linkages in soft magnetic alloys¹⁹⁶, particularly FINEMET systems¹⁹⁸ that form Fe_3Si precipitates. Metamodels to describe the crystallization of Fe_3Si domains and to predict mean particle radius and volume fraction as a function of composition, temperature and holding time were

trained on CALPHAD data as an alternative to computationally more expensive Thermo-Calc modelling. The standard FINEMET composition was varied according to $\text{Fe}_{72.89+x}\text{Si}_{16.21-x}\text{B}_{6.9}\text{Nb}_3\text{Cu}_1$, with $-3 < x < 3$. Errors relative to Thermo-Calc were generally small (<1%), with the largest errors occurring for volume fraction for short annealing times (~15%), owing to the small volume fraction leading to large relative errors.

On-the-fly ML was used to analyse X-ray diffraction data from combinatorial synthesis of Fe–Co–X (X = Mo, W, Ta, Zr, Hf, V) films to find phases with strong magnetic anisotropy¹⁹⁵. Mean shift theory, a clustering method based on non-parametric density estimation, was used to group X-ray diffraction data into similar phase regions. Non-negative matrix factorization was used to identify the fraction of different phases present in multi-phase X-ray diffraction spectra and, thus, build phase diagrams. The $\text{Fe}_{78}\text{Co}_{11}\text{Mo}_{11}$ composition was found to have an increased coercive field (FIG. 3e): a genetic algorithm search found a low-energy P4/m tetragonal structure with a matching X-ray diffraction pattern.

The Curie temperatures of magnetic materials were predicted using RFs, NNs, ridge and kernel ridge regressions¹⁹⁷. RFs were found to work best, with R^2 of 0.81 for cross-validation and 0.87 for testing. The absolute error was 57 K and the models were generally more accurate for $T_C > 300$ K. The model accurately predicted trends for the Co–Mn, Fe–Ni and Ni–Rh systems. When applied to the Al–Co–Fe system (FIG. 3f), the model underestimated the T_C of the ternary Heusler compounds but ordered them correctly.

Materials properties

This section illustrates the uses of ML for research in alloy processing, and mechanical and thermal properties (TABLE 3).

Metallurgical alloy processing

Supervised learning algorithms can be used to construct phenomenological processing–property relationships that, in many cases, have greater predictive accuracy than commonly used physical approximations. Some of the earliest examples of the application of ML to alloys are in predicting flow stress as a function of temperature, strain and strain rate. A multilayer NN was used to predict the flow stress of medium carbon steel, and its predictions were more accurate than those of a semi-empirical constitutive model¹⁹⁹. At around the same time, a NN approach was developed to predict the cold rolling force for steel based on the Bland–Ford–Ellis model²⁰⁰. Several groups have subsequently successfully applied NN methods to construct relationships between processing parameters and physical properties for other alloys^{201–207} (for example, hot deformation behaviour of the A356 aluminium alloy; FIG. 4a). The success of the NN approach can be attributed to its ability to flexibly interpolate a curve, which allows it to account for phenomena that show up empirically (in the training data) but may not be well captured by simplified physical models.

ML has also been successfully used to predict the phase evolution and distribution in alloys as a function of processing parameters. A NN model was developed

that could accurately predict the volume fractions of the α and β phases in Ti alloys as a function of heat treatment temperature and composition²⁰⁸. NNs were used to model time–temperature–transformation diagrams for Ti alloys^{60,61}, particularly for the α (hcp) to β (bcc) phase transition, to predict the processing–microstructure–property relationship. Inputs were chemical compositions and the outputs were time–temperature–transformation diagrams and the martensite start temperature. Sn, Cr and V were observed to increase martensite start time and reduce the start temperature, whereas Al increased start temperature and reduced start time, and the effect of Mo was not systematic. A model was trained to predict mechanical properties⁶¹, including tensile strength, elongation, reduction in area, fatigue strength and fracture toughness, where the inputs were composition and heat treatment type. Increased temperature reduced tensile strength and increased elongation, and hardness increased with Al content.

Bayesian NNs²⁰⁹ and Gaussian processes²¹⁰ were used to model austenite formation in steel. Model inputs consisted of the heating rate and the fractions of different elements, and the outputs were the austenite onset and completion temperatures. A maximum in the ratio of onset/completion temperature to heating rate was attributed to the presence of retained austenite: high heating rates cause the austenite onset temperature to be reached before the retained austenite has time to transition to ferrite. The austenite onset temperature falls with increasing carbon content and the completion temperature goes through a minimum at the eutectoid temperature. The onset and completion temperatures increase with Mo, Nb, Ti and V concentration and decrease with Mn and Cu concentration, whereas the effects of Co, W, B, N and P are small. The NN erroneously predicted that Ni would increase the onset temperature, but this was corrected by the Gaussian process models. The best NN had a better root-mean-square error than Gaussian processes, but this network was selected from a set of models that were generally worse.

NNs were trained to predict the martensite start temperature and austenite stabilization in steels as a function of composition and austenite grain size^{211,212}. Models were tested on 12Cr-1Mo and 9Cr-Mo high-alloy steels²¹¹ and high-strength low-alloy steels²¹². The martensite start temperature was predicted to decrease with Mn, Ni and C concentration and to increase with Co, Mo, V and Nb concentration; these results were generally consistent with MTDATA thermodynamic modelling²¹³. W inclusion was predicted to increase the start temperature, in contrast with experiments. Martensite start temperature increased with increasing austenite grain size. Low carbon content resulted in a higher austenite temperature to get the same grain size, resulting in fewer defects and, thus, easier martensite transitions.

In recent years, there has been an interest in using ML to optimize additive manufacturing processes. The additive manufacturing of stainless steel was optimized by developing a Gaussian process model that could predict the porosity of a material as a function of selective laser melting parameters²¹⁴ (FIG. 4b). Gaussian processes have also been used to predict the remelted depth of

Table 3 | Overview of machine learning applications for metallurgical processing, and mechanical and thermal properties

Year	Description	Refs
Metallurgical processing		
1995	NNs to predict flow stress of medium carbon steel	199
1996	NNs to predict cold rolling force for steel based on the Bland–Ford–Ellis model	200
1996, 1999	Bayesian NNs and Gaussian processes to model austenite formation in steel	209,210
1999–2013	NN methods to construct relationships between processing parameters and physical properties for alloys	201–207
2000, 2004	NNs to model properties including time–temperature–transformation diagrams for Ti alloys	60,61
2002, 2003	NNs to predict martensite start temperature and austenite stabilization in steels as a function of composition and austenite grain size	211,212
2015	NN model to predict volume fractions of α and β phases in Ti alloys as a function of heat treatment temperature and composition	208
2016	Gaussian process model to predict porosity in stainless steel created by additive manufacturing	214
2016	ML to accelerate characterization of alloy microstructure	219
2017	ML to guide choice of processing conditions to dramatically reduce number of trials	218
2018, 2020	Gaussian processes to predict remelted depth of powder-bed-fused stainless steel as a function of laser power and scan speed	215,216
2019	Deep convolutional NNs to automate microstructure image segmentation in high-carbon stainless steels	220
Mechanical properties		
1999	NNs and neurofuzzy networks to model threshold fatigue in Ni superalloys	231
1999	Bayesian framework NNs to design ferritic creep-resistant steels	232
2001	NNs to predict strength, ductility, hardness and toughness for Ti alloys	202
2004	NNs to predict strength, ductility, hardness and toughness for maraging steels	203
2004	NNs to optimize Charpy-impact toughness for welds	226
2005	NNs to predict strength and ductility for alloy steels	222
2007	NN and genetic algorithms to design a transformation-induced plasticity steel with low Si content	242
2008	NNs to predict strength, ductility and hardness for steels	223
2009	NNs to predict strength and ductility for Cu alloys	224
2009	NNs and orthogonal design to optimize wear resistance of chromium white cast iron	228
2013	SVMs to model wear in ‘flotation balls’ used for milling Cu ore	229
2013	NNs to model ductile damage in steel	247
2016, 2017	General ML models for elastic properties trained on data calculated from first principles	48,49,221
2016	NNs, k-nearest neighbours, classification and regression trees, and SVMs to predict strength and ductility for cast iron	225
2017	NNs to predict strength and ductility for Al alloys	234
2017	ML methods including RFs, SVMs and NNs to predict stacking fault energy in austenitic steels	244
2017, 2018	Bayesian networks to model crack formation and propagation in β -Ti alloys	235,236
2018	NNs to design hard Mo-based alloys for forging die applications	227
2018	Linear regression and principal component analysis to model fatigue in polycrystalline Ti alloys	230
2018	ML methods to infer the intrinsic mechanical material properties from indentation measurements	240
2018	k-Means algorithm to classify acoustic emission waveform data to detect fractures within the Al 2043-T3 alloy	241
2018	RF classification models to identify stress hotspots (grains experiencing high stress)	245,246
2019	RF nearest neighbour, linear regression and ridge regression to model creep in stainless steel alloys	233
2019	NNs to model crack formation and propagation in steel	237
Thermal properties		
2014	Least-squares, partial least-squares, Gaussian process and support vector regression to predict melting temperatures	250
2014	RFs to predict thermal conductivity of half-Heuslers	251
2014	Classification trees to identify compositions and features leading to high thermoelectric figure of merit in half-Heuslers	253
2016	Materials recommendation engine to find promising thermoelectric materials: Heuslers $TiRu_2Ga$, $TiRu_xIn$ and $MnRu_xIn$, and ternary germanides	254
2017, 2018	RFs to predict thermodynamic stability and vibrational energies	59,252

ML, machine learning; NN, neural network; RF, random forest; SVM, support vector machine.

powder-bed-fused stainless steel as a function of laser power and scan speed^{215,216}.

One of the most promising applications of ML to alloy processing is in the automated synthesis, processing and characterization of alloys. By coupling ML algorithms with robots, a fully autonomous system can be created that efficiently develops alloys with desired properties²¹⁷. ML can be used to guide the choice of the next set of processing conditions in a way that dramatically reduces the number of trials that must be conducted before an optimal set of conditions is found²¹⁸ (FIG. 4c). Similarly, characterization can be accelerated by

using ML to minimize the number of samples that must be collected by a microscope to accurately characterize an alloy's microstructure²¹⁹. Characterization can also be automated by taking advantage of the tremendous progress that has recently been made in computer vision. For example, a deep convolutional NN was trained to automate microstructure segmentation in high-carbon stainless steels²²⁰. When combined in an automated environment, such tools have the potential to dramatically increase the efficiency of the design and discovery of new alloys and the optimization of processing conditions.

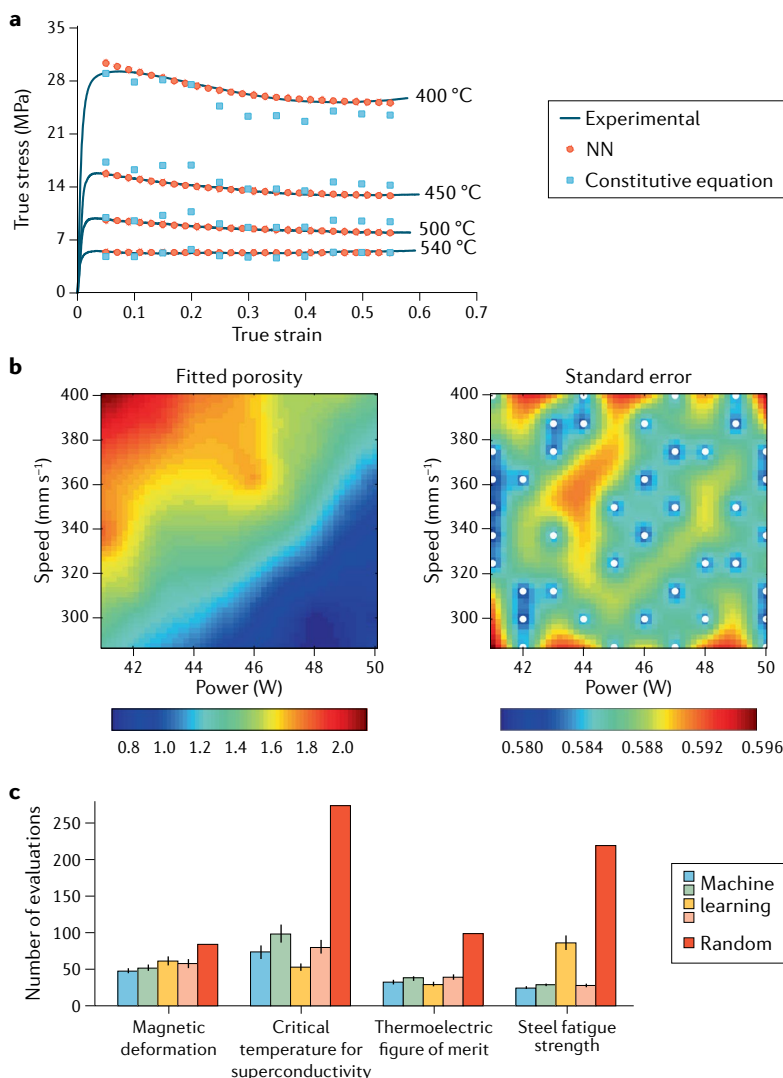


Fig. 4 | Machine learning for alloy processing. **a** Comparison between flow stresses obtained experimentally, from a neural network (NN) model and from a constitutive equation for the A356 aluminium alloy at a strain rate of 0.001 per second at different temperatures. **b** Porosity for steel materials created by additive manufacturing as predicted by a Gaussian process model trained using only the initial set of observations (left). The corresponding initial prediction standard error, with training data marked by the white dots (right). Regions with relatively high standard error were identified as those in which additional sampling would be particularly beneficial. **c** The number of trials required to find the optimal candidates for different material properties using four methods guided by machine learning, compared with random guessing (red). The steel results include both composition and process optimization. Panel **a** reprinted with permission from REF.²⁰⁷, Elsevier; panel **b** reprinted with permission from REF.²¹⁴, Elsevier; and panel **c** reprinted from REF.²¹⁸, Springer Nature Limited.

Mechanical properties

ML models have been trained to predict the mechanical properties of metal alloys, ranging from general models for elastic properties trained on data calculated from first principles^{48,49,221} to models of macroscopic properties such as hardness, toughness and strength^{202,203,222–227}, as well as phenomena such as wear^{228,229}, fatigue^{230,231}, creep^{232,233}, hydrogen embrittlement²³⁴ and crack formation and propagation^{235–237} in specific alloy systems (TABLE 3).

Elastic properties from DFT data. Models based on gradient boosting decision trees were trained on large online databases of calculations of bulk and shear moduli^{48,49}. Features included composition-averaged properties of the component elements^{48,49} and ab initio-calculated properties of the actual compound, such as the cohesive energy⁴⁸. The most predictive features included the cohesive energy and the volume per atom. Models for mechanical properties are programmatically accessible through an online application programming interface^{238,239}.

Experimental interpretation. ML models assist in the analysis and interpretation of mechanical testing methods. A combination of Gaussian process modelling, finite element analysis, Bayesian inference and Markov chain Monte Carlo was used to infer the intrinsic mechanical material properties from indentation measurements²⁴⁰. The method was applied to the Al 6061 alloy and good values were obtained for the yield stress, but estimating hardening values would have required much larger strains.

An unsupervised *k*-means algorithm was used to classify acoustic emission waveform data to detect fractures within aircraft-grade, precipitate-hardened Al 2043-T3 alloy²⁴¹. Acoustic emission data were coupled with direct fracture observation to identify waveform features corresponding with fracture formation. The data were then clustered using an unsupervised *k*-means ML algorithm to find waveforms that could be used to detect the presence of fractures.

Strength, ductility, hardness, toughness. NNs^{202,203,222–227,234,242}, *k*-nearest neighbour²²⁵, classification and regression trees²²⁵, χ^2 -square automatic interaction detection²²⁵ and SVMs²²⁵ were trained to predict mechanical properties such as tensile strength^{202,203,222–225,234}, yield strength^{202,203,223–225,227,234}, elongation^{202,203,222–225,234}, reduction in area^{202,203,222,223}, hardness^{202,203,223,227} fracture toughness^{202,203} and impact

toughness^{203,226} of steels^{203,222,223,242}, cast iron²²⁵, welds²²⁶ and Ti-based²⁰², Cu-based²²⁴, Al-based²³⁴ and Mo-based²²⁷ alloys. Input features included alloy compositions along with processing and testing parameters, such as cold deformation degree²⁰³, ageing temperature and time²⁰³, heat treatment temperature and time^{202,234}, testing temperature^{202,226} and welding parameters, such as heat input and interpass temperature²²⁶. Training data were extracted from literature sources such as the CASTI Metals books and the ASM handbooks, or were generated by experimental synthesis and characterization²²⁵.

The models were used to explore the effects of composition and processing on the mechanical properties of alloys and were used in conjunction with optimization algorithms to design new materials with enhanced properties. A model for the properties of maraging steels²⁰³ was able to predict the effect of Co–Mo interactions on martensite start temperature and hardness, as well as the optimum composition for the C250 alloy. The model also predicted that Cu speeds up age hardening by nucleating precipitate formation. Models to classify the properties of nodular cast iron and austempered ductile iron predicted that adding carbides would increase the wear resistance of the materials, whereas the ductility of austempered ductile iron would increase with austenite content²²⁵; Cu, Mn and Cr would reduce strength, whereas Ni would increase it. An ensemble of ten NNs were trained on industrial data to predict the strength and ductility of alloy steels as a function of composition and tempering temperature²²². Multiobjective optimization was performed to find the Pareto-optimal solution, using the strength Pareto evolutionary algorithm to simultaneously optimize the tensile strength, the reduction in area and elongation, and their standard deviations. For high-temperature Ti-based alloys, the mechanical properties were predicted to be generally stable up to around 500 °C and start to degrade above 600 °C, which was in agreement with experimental observations, whereas the alloying elements Al and V were predicted to increase tensile strength and reduce elongation²⁰².

A transformation-induced plasticity steel with low Si content was designed using NNs and genetic algorithms²⁴². The concentration of all elements except P in the Fe–C–Mn–Si–Al–Mo–Cu alloy system was varied, and different treatment temperatures were investigated. Dendrites of δ-ferrite were found to form, replacing the allotriomorphic ferrite instead of retaining austenite. Uniform elongation by 23% was observed (no necking) by strain-induced transformation of retained austenite to martensite.

NN models were combined with optimization algorithms to maximize the Charpy impact toughness of welds²²⁶. When varying the Ni, Mn and C concentrations, the linear optimizer failed to find the optimum, whereas the other methods predicted a composition with a toughness of 87 ± 20 J (the experimental value was measured to be 101 J). Varying the concentration of all 13 components using a local/hybrid optimizer, which explored the composition space more thoroughly than other methods, produced a composition with an increased interpass temperature (300 °C), a Charpy

toughness of 86 ± 20 J at –60 °C and a room-temperature yield strength of 840 ± 105 MPa.

NNs were used to optimize the yield stress and hardness of Mo-based alloys for forging die applications²²⁷ and were trained using CALPHAD/SSOL6 data to predict phase stability. The logarithm of likelihood was maximized so that the optimizer improved the least optimized property, and the composition space was explored in a random walk. The new alloy had a predicted yield stress of 722 MPa, a hardness of 2.274 GPa (232 HV) and a cost of \$42 per cycle, which is less than the current least expensive alloy, TZC, at \$52 per cycle. Synthesis and experimental testing indicated that the alloy had 4 wt% HfC, a Mo-rich matrix, was thermally stable and had properties similar to those predicted by ML.

RFs, linear least square, *k*-nearest neighbour and NN regression were used to predict fatigue strength, fracture strength, tensile strength and hardness of steels²⁴³, and symbolic regression was combined with genetic programming to generate equations describing these properties as a function of composition and tempering temperature. RFs worked best for predicting fracture strength, NNs for the other properties.

Stacking fault energy. Several different methods, including RFs, SVMs and NNs, were used to predict the stacking fault energy in austenitic steels²⁴⁴. This energy determines plastic deformation mechanisms: a value below 20 mJ m^{–2} results in transformation-induced plasticity in the form of martensitic transformations, the range 20 mJ m^{–2} to 45 mJ m^{–2} gives twinning-induced plasticity, whereas slip processes dominate for values greater than 45 mJ m^{–2}. For stacking fault energy classification, RFs were found to be slightly better than the other methods: a 10% false positive rate compared with 13% for SVMs or artificial NNs. The misclassification was primarily between low and medium or medium and high stacking fault energies, with the models being very reliable at distinguishing between low and high stacking fault energies.

Stress hotspots. Stress hotspots (grains experiencing high stress) were identified using RF classification models²⁴⁵ and different feature selection methods were compared²⁴⁶. The Schmid factor (optimal orientation of the slip system) was found to be the most important feature, with hotspots found in grains with low values. Another important feature in fcc structures was found to be the angle between the loading direction and the <100> crystal direction, and small grains were found to have higher stress²⁴⁵. Different feature selection methods were used to select the best features to build new RF models²⁴⁶. With all features, the area under the curve was 71.94%, whereas with selected features only, it was 81%, with similar accuracy for all feature selection methods. FeaLect (an improvement on LASSO) has advantages over other methods: LASSO tends to arbitrarily select one feature from a strongly correlated set, Pearson correlation assumes features are independent, recursive feature elimination and correlated feature selection do not give a quantitative ranking and RF permutation accuracy importance tends to eliminate strongly correlated

features, even if they are strongly predictive. FeaLect predicted that hcp grains oriented so that the *c*-axis is perpendicular to the strain axis tend to be stress hotspots.

Fatigue and cracking. NNs^{231,237,247}, neurofuzzy networks²³¹, Bayesian networks^{235,236} and PCA and linear regression²³⁰ were used to model fatigue^{230,231}, crack formation and propagation^{235–237}, and ductile damage²⁴⁷ in Ni superalloys²³¹, polycrystalline Ti microstructures²³⁰, β -Ti alloys^{235,236} and steel^{237,247}.

Threshold fatigue in Ni superalloys was modelled using neural and neurofuzzy networks²³¹. Large grain sizes resulted in low yield stress but also in a high fatigue threshold, owing to the associated closure effects. The necklace grain structure was found to have little effect on the models, owing to the few data points in the original set.

Bayesian networks were used to investigate crack front propagation in β -Ti alloys²³⁵, such as VST-55531 (REF.²³⁶). Fatigue indicator parameters were calculated from the micromechanical force field data, representing slip systems and strains. Analysis using Bayesian networks indicated that the different fatigue indicator parameters had similar predictive ability, except for total plasticity, which was significantly worse than the other indicators. The model was found to be reliable for predicting failure close to the crack front when residual life was low, but was untrustworthy far from the crack front. The model for VST-55531 (REF.²³⁶) was found to generally work well for intragranular crack propagation, but had problems predicting propagation across grain boundaries and needed a minimum distance to the first grain boundary to properly sample the analysed slip direction.

Deep NN models were developed to predict solidification crack susceptibility in welds in sheet metal stainless steel²³⁷. Longitudinal Varestraint test data taken from the literature included composition, welding current, voltage and velocity, applied strain and total crack length. PCA was used to reduce input data dimensionality to 15 and 10 principle components; however, this worsened the model accuracy. Pearson correlations of 0.89, 0.89 and 0.93 were obtained for the crack length test sets using SVMs, shallow NNs and a deep NN, respectively. The model also predicted the effects of Mn, Ti, N and Si on the total crack length, and a high Cr-to-Ni ratio was found to give better crack resistance.

NNs were used to determine the Gurson–Tvergaard–Needleman ductile damage parameters during sheet metal forming in steel²⁴⁷. These parameters, based on the void volume fractions and nucleation strains, were used to model the elliptical bulge test and Erichsen cupping test: the resulting finite element model identifies the location of the fracture reasonably well.

Several regression models were used to investigate the processing–composition–fatigue strength (maximum stress for a certain number of cycles before breaking) relationships for carbon, low-alloy, carburizing and spring steels^{248,249}. Training data were taken from the National Institute of Materials Science (NIMS) database and features included composition, processing details such as heat treatment conditions and mechanical properties such as yield strength and hardness. Tempering

temperature was found to be the most important feature, partly owing to high temperatures being combined with carburization steps. Other important features included carburization time and temperature, diffusion time and temperature, and quenching media temperature, with the most important element in the composition being C. An online tool has been made available for generating predictions using the models²⁴⁹.

Wear. SVMs with radial, exponential radial and polynomial basis kernels were used to model wear in ‘flotation balls’ used for milling Cu ore²²⁹, with the exponential radial basis kernels giving the lowest root-mean-square errors. The wear rate of the flotation balls was found to reduce both with increasing hardness and, in the case of low-hardness compositions, with increasing Mn content.

NNs combined with orthogonal design were used to optimize the wear resistance of chromium white cast iron²²⁸. Cu was found to be the most important element, then Si, Mn and Cr. An expression for the wear rate was obtained using quadratic regression in addition to the NN model. For an additional data set generated for testing, the quadratic regression model had a maximum error of 188.2%, whereas the error for the NN was just 3.1%, indicating that the NN was much more generally applicable when it came to predicting behaviour outside of the training set.

Creep. Creep in stainless steel alloys was modelled using RF, nearest neighbour, linear regression, kernel ridge regression and Bayesian ridge regression²³³. Pearson correlation and maximum information correlation were used for feature selection, with stress and creep test temperature found to be the most important. All models except for kernel ridge regression had accuracy greater than 90% when trained with just composition and stress. With all features included, only RF, nearest neighbour and Bayesian ridge regression had accuracy above 90%.

Bayesian NNs were used to design ferritic creep-resistant steels²³². Data were extracted from the literature for Fe–2.25Cr–1Mo (a bainitic steel for use up to 565°C) and Fe–(9–12)Cr (a martensitic steel). Input variables included composition, heat treatment type, temperature, duration and cooling rate, and the output was the rupture stress as a function of time and temperature. 10CrMoW was correctly predicted by the model to have a higher rupture stress than 2.25Cr–1Mo. Error bars were larger for 10CrMoW and for higher rupture times, owing to less data availability. Co was found to increase strength, Ni and Al to reduce it. Cu and W tend to form a Laves phase intermetallic, weakening the material, but W without Cu increases strength. Two new steel compositions were proposed, with more W and no Cu, Ni, Al or Si.

Thermal properties

ML has been applied to predict thermal properties, including melting temperature²⁵⁰, thermal conductivity²⁵¹, vibrational energy contribution to thermodynamic stability^{252,253} and the thermoelectric figure of merit (zT)^{253,254}. Four types of regression were compared for predicting melting temperature²⁵⁰: least squares, partial least squares, Gaussian process and support vector.

Support vector regression gave the best predictions for single-component and binary-component solids. RFs were leveraged in 2014 (REF.²⁵⁵) to optimize the thermal conductivity of half-Heuslers²⁵¹. In 2017, Natalio Mingo and colleagues presented a very interesting comparison: experiments versus ab initio results²⁵². The authors trained RFs to predict the stability of experimentally reported half-Heusler compounds and compared the results with several ab initio studies. Some inconsistencies were found and were attributed to factors beyond those considered by usual ab initio phase stability calculations based on formation enthalpies. To enhance prediction power at finite temperatures, RFs were also used to address phonon spectral features, heat capacities, vibrational entropies and vibrational free energies⁵⁹.

ML approaches were used to search for materials with a high thermoelectric figure of merit^{253,254}. Classification trees were used to identify compositions and features leading to high zT in half-Heuslers²⁵³. Large lattice parameters and a wide band gap (at high temperatures) or large hole effective mass (at room temperature) tended to produce high zT . A ML recommendation engine (thermoelectrics.citrination.com) was used to find materials with a high zT (REF.²⁵⁴). Promising candidates included Heusler structures with compositions TiRu_2Ga , TiRu_2In and MnRu_2In , as well as ternary germanides such as materials in the Mn–Ru–Ge and Dy–Ru–Ge systems.

Future directions

ML will play an essential role in addressing challenges that are too difficult for traditional modelling. Going forwards, it is particularly likely to have a large impact in the following areas.

Autonomous materials design

Autonomous design and optimization will combine ML with active learning to choose synthesis priorities^{2,144} and will include generative models for materials prediction. By balancing exploration (gathering new data in areas where data are sparse) with exploitation (searching for optimal properties), automated machinery will be capable of generating large volumes of high-quality experimental data by running around the clock.

Complex problems

The unavoidability of disorder in systems with a large number of species³⁷ will require the use of ML for the development of industrial superalloys and high-entropy systems^{106,256}. Similarly, ML will be the key to understanding systems where direct modelling of processes and properties is too expensive, such as glass formation^{89,90} or magnetic ordering^{193,194,197}. The characterization of grain boundary chemistry for its role in corrosion processes, microstructure kinetics and plasticity is another very difficult problem that is already being tackled by ML. Methods such as symbolic regression may yield human-interpretable models that provide new insights into the fundamental factors governing the behaviour of complex systems^{68,257,258}. Similarly, NNs such as autoencoders may be used to find compact latent representations with physically interpretable variables^{259,260}.

Machine-learned force fields

The development of general-purpose interatomic potentials is one of the most promising applications of ML to alloy research. These potentials can extend simulation timescales and length scales, and, via active learning, achieve predictive accuracy comparable with that of ab initio calculations. We anticipate that such models will be used to simulate increasingly realistic systems (such as polycrystalline materials, composites, interfaces, microstructures, materials with defects and surfaces) and, eventually, to accelerate the development of new alloy-based technologies. To such extent, continued innovation will be necessary to improve accuracy, training and performance speeds. In particular, advances in active learning, regularization and the identification of compact, physically meaningful representations are likely to have significant impact.

Quantum calculations

DFT, one of the most successful and widely used methods in atomic-scale alloy modelling, relies on approximations to calculate material properties from first principles. These approximations include the use of an approximate exchange-correlation functional (as the exact form remains unknown) and the use of pseudopotentials or projector-augmented waves. The speed and accuracy of a DFT calculation depends, to a large extent, on the quality of these approximations. ML holds the promise of improving these methods by systematically fitting them to highly accurate experimental and/or computational data, while satisfying known physical constraints². The use of ML to generate exchange-correlation functionals is emerging as a particularly active field of research^{261–264}.

Data standardization and integration

ML requires large data sets of both positive and negative results for training and testing, generated using consistent methodologies and distributed in standardized, interoperable formats. To address the latter issue — the variety of interfaces and formats used by materials databases — the Open Databases Integration for Materials Design (OPTIMADE) consortium has developed a universal application programming interface²⁶⁵, providing a common search syntax and a standardized output format. The Novel Materials Discovery (NOMAD) repository⁴⁴ aggregates materials data from multiple sources to create a centralized resource.

Delta learning

Models trained on the differences between large sets of inexpensive, low-fidelity data and small sets of high-fidelity data (for example, using computational methods that go beyond local density approximate/generalized gradient approximation or experimental means) can be used to ‘bootstrap’ the larger database to the higher fidelity level of the smaller one. The model learns the difference by fitting to the entries common to both data sets. The outcome is a ML model that can make predictions consistent with the physics included in the more expensive method. Delta learning has already been tested in a handful of cases and will

develop into a standard method in the toolbox of the materials scientist²⁶⁶.

Conclusions

ML is a revolutionary tool in alloy research. It is enabling a metallurgical renaissance. Combined with databases and high-throughput characterization, this approach can already solve outstanding materials

problems. In this Review, we have briefly described the state of the field and analysed several concepts, methods and applications. The partnership between ML and alloy research will rapidly adapt to the challenges waiting at the horizon and continue its unstoppable momentum.

Published online 20 July 2021

1. Butler, K. T., Davies, D. W., Cartwright, H., Isayev, O. & Walsh, A. Machine learning for molecular and materials science. *Nature* **559**, 547–555 (2018).
2. Schmidt, J., Marques, M. R. G., Botti, S. & Marques, M. A. L. Recent advances and applications of machine learning in solid-state materials science. *NPJ Comput. Mater.* **5**, 83 (2019).
3. Muratov, E. N. et al. QSAR without borders. *Chem. Soc. Rev.* **49**, 3525–3564 (2020).
4. Curtarolo, S. et al. The high-throughput highway to computational materials design. *Nat. Mater.* **12**, 191–201 (2013).
5. Tanaka, I., Rajan, K. & Wolverton, C. Data-centric science for materials innovation. *MRS Bull.* **43**, 659–665 (2018).
6. Behler, J. Atom-centered symmetry functions for constructing high-dimensional neural network potentials. *J. Chem. Phys.* **134**, 074106 (2011).
7. Rupp, M., Tkatchenko, A., Müller, K.-R. & von Lilienfeld, O. A. Fast and accurate modeling of molecular atomization energies with machine learning. *Phys. Rev. Lett.* **108**, 058301 (2012).
8. Bartók, A. P., Kondor, R. & Csányi, G. On representing chemical environments. *Phys. Rev. B* **87**, 184115 (2013).
9. Bartók, A. P., Payne, M. C., Kondor, R. & Csányi, G. Gaussian approximation potentials: The accuracy of quantum mechanics, without the electrons. *Phys. Rev. Lett.* **104**, 136403 (2010).
10. Huang, B. & von Lilienfeld, O. A. Communication: Understanding molecular representations in machine learning: The role of uniqueness and target similarity. *J. Chem. Phys.* **145**, 161102 (2016).
11. Shapeev, A. V. Moment tensor potentials: A class of systematically improvable interatomic potentials. *Multiscale Model. Simul.* **14**, 1153–1173 (2016).
12. Drautz, R. Atomic cluster expansion for accurate and transferable interatomic potentials. *Phys. Rev. B* **99**, 014104 (2019).
13. Pozdnyakov, S. N. et al. Incompleteness of atomic structure representations. *Phys. Rev. Lett.* **125**, 166001 (2020).
14. Faber, F., Lindmaa, A., von Lilienfeld, O. A. & Armiento, R. Crystal structure representations for machine learning models of formation energies. *Int. J. Quantum Chem.* **115**, 1094–1101 (2015).
15. Zhang, L., Han, J., Wang, H., Car, R. & Weinan, E. Deep potential molecular dynamics: A scalable model with the accuracy of quantum mechanics. *Phys. Rev. Lett.* **120**, 143001 (2018).
16. Bach, S. et al. On pixel-wise explanations for non-linear classifier decisions by layer-wise relevance propagation. *PLoS One* **10**, e0130140 (2015).
17. Montavon, G., Samek, W. & Müller, K.-R. Methods for interpreting and understanding deep neural networks. *Digit. Signal. Process.* **73**, 1–15 (2018).
18. Lapuschkin, S. et al. Unmasking Clever Hans predictors and assessing what machines really learn. *Nat. Commun.* **10**, 1096 (2019).
19. Rosenbrock, C. W., Homer, E. R., Csányi, G. & Hart, G. L. W. Discovering the building blocks of atomic systems using machine learning: application to grain boundaries. *NPJ Comput. Mater.* **3**, 29 (2017).
20. Schütt, K. T., Arbabzadah, F., Chmiela, S., Müller, K. R. & Tkatchenko, A. Quantum-chemical insights from deep tensor neural networks. *Nat. Commun.* **8**, 13890 (2017).
21. Schaffer, J. P., Saxena, A., Antolovich, S. D., Sanders, T. H. Jr. & Warner, S. B. *The Science and Design of Engineering Materials* 2nd edn. (WCB/McGraw-Hill, 1999).
22. Callister, W. D., Jr. & Rethwisch, D. G. *Materials Science and Engineering: An Introduction* 10th edn. (Wiley, 2018).
23. Wei, S.-H., Ferreira, L. G. & Zunger, A. First-principles calculation of temperature-composition phase diagrams of semiconductor alloys. *Phys. Rev. B* **41**, 8240 (1990).
24. Pan, J. et al. Perfect short-range ordered alloy with line-compound-like properties in the ZnSnN_x/ZnO system. *NPJ Comput. Mater.* **6**, 63 (2020).
25. Stevanović, V., Zakutayev, A. & Lany, S. Composition dependence of the band gap and doping in Cu₂O-based alloys as predicted by an extension of the dilute-defect model. *Phys. Rev. Appl.* **2**, 044005 (2014).
26. Jiang, J., Chen, M. & Fan, J. A. Deep neural networks for the evaluation and design of photonic devices. *Nat. Rev. Mater.* **10**.1038/s41578-020-00260-1 (2020).
27. Vasudevan, R., Pilania, G. & Balachandran, P. V. Machine learning for materials design and discovery. *J. Appl. Phys.* **129**, 070401 (2021).
28. Hastie, T., Tibshirani, R. & Friedman, J. H. *The Elements of Statistical Learning: Data Mining, Inference, and Prediction* (Springer, 2001).
29. Batra, R., Song, L. & Ramprasad, R. Emerging materials intelligence ecosystems propelled by machine learning. *Nat. Rev. Mater.* **10**.1038/s41578-020-00255-y (2020).
30. Mueller, T., Kusne, A. G. & Ramprasad, R. Machine learning in materials science: Recent progress and emerging applications. *Rev. Comput. Chem.* **29**, 186–273 (2016).
31. Gubernatis, J. E. & Lookman, T. Machine learning in materials design and discovery: Examples from the present and suggestions for the future. *Phys. Rev. Mater.* **2**, 120301 (2018).
32. Kalidindi, S. R. Feature engineering of material structure for AI-based materials knowledge systems. *J. Appl. Phys.* **128**, 041103 (2020).
33. Sanchez, J. M., Ducastelle, F. & Gratias, D. Generalized cluster description of multicomponent systems. *Phys. A* **128**, 334–350 (1984).
34. de Fontaine, D. in *Solid State Physics Vol. 47* (eds Ehrenreich, H. & Turnbull, D.) 33–176 (Academic Press, 1994).
35. Hart, G. L. W., Curtarolo, S., Massalski, T. B. & Levy, O. Comprehensive search for new phases and compounds in binary alloy systems based on platinum-group metals, using a computational first-principles approach. *Phys. Rev. X* **3**, 041035 (2013).
36. Oses, C. et al. AFLOW-CHULL: Cloud-oriented platform for autonomous phase stability analysis. *J. Chem. Inf. Model.* **58**, 2477–2490 (2018).
37. Toher, C., Oses, C., Hicks, D. & Curtarolo, S. Unavoidable disorder and entropy in multi-component systems. *NPJ Comput. Mater.* **5**, 69 (2019).
38. Sarker, P. et al. High-entropy high-hardness metal carbides discovered by entropy descriptors. *Nat. Commun.* **9**, 4980 (2018).
39. Yong, J. et al. Robust topological surface state of kondo insulator SmB₆ thin films. *Appl. Phys. Lett.* **105**, 222403 (2014).
40. Bergerhoff, G., Hundt, R., Sievers, R. & Brown, I. D. The inorganic crystal structure data base. *J. Chem. Inf. Comput. Sci.* **23**, 66–69 (1983).
41. Curtarolo, S. et al. AFLOW: An automatic framework for high-throughput materials discovery. *Comput. Mater. Sci.* **51**, 218–226 (2012).
42. Saal, J. E., Kirklin, S., Aykol, M., Meredig, B. & Wolverton, C. Materials design and discovery with high-throughput density functional theory: The Open Quantum Materials Database (OQMD). *JOM* **65**, 1501–1509 (2013).
43. Jain, A. et al. A high-throughput infrastructure for density functional theory calculations. *Comput. Mater. Sci.* **50**, 2295–3310 (2011).
44. Draxl, C. & Scheffler, M. NOMAD: The FAIR concept for big data-driven materials science. *MRS Bull.* **43**, 676–682 (2018).
45. van de Walle, A. & Ceder, G. Automating first-principles phase diagram calculations. *J. Phase Equilib.* **23**, 348–359 (2002).
46. Hart, G. L. W., Blum, V., Walorski, M. J. & Zunger, A. Evolutionary approach for determining first-principles hamiltonians. *Nat. Mater.* **4**, 391–394 (2005).
47. Nelson, L. J., Hart, G. L. W., Zhou, F. & Ozoliņš, V. Compressive sensing as a paradigm for building physics models. *Phys. Rev. B* **87**, 035125 (2013).
48. de Jong, M. et al. A statistical learning framework for materials science: Application to elastic moduli of *k*-nary inorganic polycrystalline compounds. *Sci. Rep.* **6**, 34256 (2016).
49. Isayev, O. et al. Universal fragment descriptors for predicting properties of inorganic crystals. *Nat. Commun.* **8**, 15679 (2017).
50. Koinuma, H. & Takeuchi, I. Combinatorial solid-state chemistry of inorganic materials. *Nat. Mater.* **3**, 429–438 (2004).
51. Jóhannesson, G. H. et al. Combined electronic structure and evolutionary search approach to materials design. *Phys. Rev. Lett.* **88**, 255506 (2002).
52. Ceder, G., Morgan, D., Fischer, C., Tibbetts, K. & Curtarolo, S. Data-mining driven quantum mechanics for the prediction of structure. *MRS Bull.* **31**, 981–985 (2006).
53. Curtarolo, S., Morgan, D. & Ceder, G. Accuracy of ab initio methods in predicting the crystal structures of metals: A review of 80 binary alloys. *Calphad* **29**, 163–211 (2005).
54. Bligaard, T. et al. Pareto-optimal alloys. *Appl. Phys. Lett.* **83**, 4527–4529 (2003).
55. Fischer, C. C., Tibbetts, K. J., Morgan, D. & Ceder, G. Predicting crystal structure by merging data mining with quantum mechanics. *Nat. Mater.* **5**, 641–646 (2006).
56. Villars, P. et al. *Crystal Impact, Pauling File, Inorganic Materials Database and Design System, Binaries Edition* (ASM International, 2003).
57. Hautier, G., Fischer, C., Ehrlacher, V., Jain, A. & Ceder, G. Data mined ionic substitutions for the discovery of new compounds. *Inorg. Chem.* **50**, 656–663 (2011).
58. Suh, C. & Rajan, K. Data mining and informatics for crystal chemistry: establishing measurement techniques for mapping structure-property relationships. *Mater. Sci. Technol.* **25**, 466–471 (2009).
59. Legrain, F. et al. Vibrational properties of metastable polymorph structures by machine learning. *J. Chem. Inf. Model.* **58**, 2460–2466 (2018).
60. Malinov, S., Sha, W. & Guo, Z. Application of artificial neural network for prediction of time-temperature-transformation diagrams in titanium alloys. *Mater. Sci. Eng. A* **283**, 1–10 (2000).
61. Malinov, S. & Sha, W. Application of artificial neural networks for modelling correlations in titanium alloys. *Mater. Sci. Eng. A* **365**, 202–211 (2004).
62. Liu, S. et al. Physics-informed machine learning for composition–process–property design: Shape memory alloy demonstration. *Appl. Mater. Today* **22**, 100898 (2021).
63. Schütt, K. T. et al. How to represent crystal structures for machine learning: Towards fast prediction of electronic properties. *Phys. Rev. B* **89**, 205118 (2014).
64. Sutton, C. et al. Crowd-sourcing materials-science challenges with the NOMAD 2018 Kaggle competition. *NPJ Comput. Mater.* **5**, 111 (2019).
65. Xie, T. & Grossman, J. C. Crystal graph convolutional neural networks for an accurate and interpretable prediction of material properties. *Phys. Rev. Lett.* **120**, 145301 (2018).
66. Chen, C., Yé, W., Zuo, Y., Zheng, C. & Ong, S. P. Graph networks as a universal machine learning framework for molecules and crystals. *Chem. Mater.* **31**, 3564–3572 (2019).
67. Non, J. et al. Inverse design of solid-state materials via a continuous representation. *Matter* **1**, 1370–1384 (2019).
68. Schmidt, M. & Lipson, H. Distilling free-form natural laws from experimental data. *Science* **324**, 81–85 (2009).

69. Ghiringhelli, L. M., Vybird, J., Levchenko, S. V., Draxl, C. & Scheffler, M. Big data of materials science: Critical role of the descriptor. *Phys. Rev. Lett.* **114**, 105503 (2015).
70. Ouyang, R., Curtarolo, S., Ahmetcik, E., Scheffler, M. & Ghiringhelli, L. M. SISSO: A compressed-sensing method for identifying the best low-dimensional descriptor in an immensity of offered candidates. *Phys. Rev. Mater.* **2**, 083802 (2018).
71. Yuan, F. & Mueller, T. Identifying models of dielectric breakdown strength from high-throughput data via genetic programming. *Sci. Rep.* **7**, 17594 (2017).
72. Udrescu, S.-M. & Tegmark, M. Al Feynman: A physics-inspired method for symbolic regression. *Sci. Adv.* **6**, eaay2631 (2020).
73. Owolabi, T. O., Akande, K. O. & Olatunji, S. O. Prediction of superconducting transition temperatures for Fe-based superconductors using support vector machine. *Adv. Phys. Theor. Appl.* **35**, 12–26 (2014).
74. Owolabi, T. O., Akande, K. O. & Olatunji, S. O. Estimation of superconducting transition temperature T_c for superconductors of the doped MgB₂ system from the crystal lattice parameters using support vector regression. *J. Supercond. Nov. Magn.* **28**, 75–81 (2015).
75. Isayev, O. et al. Materials cartography: representing and mining materials space using structural and electronic fingerprints. *Chem. Mater.* **27**, 735–743 (2015).
76. Stanev, V. et al. Machine learning modeling of superconducting critical temperature. *NPJ Comput. Mater.* **4**, 29 (2018).
77. Kusne, A. G. et al. On-the-fly closed-loop materials discovery via Bayesian active learning. *Nat. Commun.* **11**, 5966 (2020).
78. Cheng, Y. Q. & Ma, E. Atomic-level structure and structure–property relationship in metallic glasses. *Prog. Mater. Sci.* **56**, 379–473 (2011).
79. Zberg, B., Uggowitzer, P. J. & Löffler, J. F. MgZnCa glasses without clinically observable hydrogen evolution for biodegradable implants. *Nat. Mater.* **8**, 887–891 (2009).
80. Inoue, A. Stabilization of metallic supercooled liquid and bulk amorphous alloys. *Acta Mater.* **48**, 279–306 (2000).
81. Miracle, D. B. A structural model for metallic glasses. *Nat. Mater.* **3**, 697–702 (2004).
82. Sheng, H. W., Luo, W. K., Alamgir, F. M., Bai, J. M. & Ma, E. Atomic packing and short-to-medium-range order in metallic glasses. *Nature* **439**, 419–425 (2006).
83. Laws, K. J., Miracle, D. B. & Ferry, M. A predictive structural model for bulk metallic glasses. *Nat. Commun.* **6**, 8123 (2015).
84. Lu, Z. P. & Liu, C. T. A new glass-forming ability criterion for bulk metallic glasses. *Acta Mater.* **50**, 3501–3512 (2002).
85. Mondal, K. & Murty, B. S. On the parameters to assess the glass forming ability of liquids. *J. Non-Cryst. Solids* **351**, 1366–1371 (2005).
86. Cheney, J. & Vecchio, K. S. Prediction of glass-forming compositions using liquidus temperature calculations. *Mater. Sci. Eng. A* **471**, 135–143 (2007).
87. Perim, E. et al. Spectral descriptors for bulk metallic glasses based on the thermodynamics of competing crystalline phases. *Nat. Commun.* **7**, 12315 (2016).
88. Ford, D. C., Hicks, D., Oses, C., Toher, C. & Curtarolo, S. Metallic glasses for biodegradable implants. *Acta Mater.* **176**, 297–305 (2019).
89. Ward, L., Agrawal, A., Choudhary, A. & Wolverton, C. A general-purpose machine learning framework for predicting properties of inorganic materials. *NPJ Comput. Mater.* **2**, 16028 (2016).
90. Ren, F. et al. Accelerated discovery of metallic glasses through iteration of machine learning and high-throughput experiments. *Sci. Adv.* **4**, eaq1566 (2018).
91. Ward, L. et al. A machine learning approach for engineering bulk metallic glass alloys. *Acta Mater.* **159**, 102–111 (2018).
92. Sun, Y. T., Bai, H. Y., Li, M. Z. & Wang, W. H. Machine learning approach for prediction and understanding of glass-forming ability. *J. Phys. Chem. Lett.* **8**, 3434–3439 (2017).
93. Dasgupta, A. et al. Probabilistic assessment of glass forming ability rules for metallic glasses aided by automated analysis of phase diagrams. *Sci. Rep.* **9**, 357 (2019).
94. Tripathi, M. K., Chattopadhyay, P. P. & Ganguly, S. Multivariate analysis and classification of bulk metallic glasses using principal component analysis. *Comput. Mater. Sci.* **107**, 79–87 (2015).
95. Keong, K. G., Sha, W. & Malinov, S. Artificial neural network modelling of crystallization temperatures of the Ni–P based amorphous alloys. *Mater. Sci. Eng. A* **365**, 212–218 (2004).
96. Cai, A.-H., Wang, H., Li, X.-S., Chen, H. & An, W.-K. Progress of component design methods for bulk metallic glass. *Mater. Des.* **28**, 2694–2697 (2007).
97. Cai, A.-H., Xiong, X., Liu, Y., An, W.-K. & Tan, J.-Y. Artificial neural network modeling of reduced glass transition temperature of glass forming alloys. *Appl. Phys. Lett.* **92**, 111909 (2008).
98. Cai, A.-H. et al. Artificial neural network modeling for undercooled liquid region of glass forming alloys. *Comput. Mater. Sci.* **48**, 109–114 (2010).
99. Cai, A. H. et al. Prediction of critical cooling rate for glass forming alloys by artificial neural network. *Mater. Des.* **52**, 671–676 (2013).
100. Xiong, J., Zhang, T.-Y. & Shi, S.-Q. Machine learning prediction of elastic properties and glass-forming ability of bulk metallic glasses. *MRS Commun.* **9**, 576–585 (2019).
101. Fang, S., Xiao, X., Xia, L., Li, W. & Dong, Y. Relationship between the widths of supercooled liquid regions and bond parameters of Mg-based bulk metallic glasses. *J. Non-Cryst. Solids* **321**, 120–125 (2003).
102. Xiong, J., Shi, S.-Q. & Zhang, T.-Y. A machine-learning approach to predicting and understanding the properties of amorphous metallic alloys. *Mater. Des.* **187**, 108378 (2020).
103. Kawazoe, Y., Yu, J.-Z., Tsai, A.-P. & Masumoto, T. (eds) *Nonequilibrium Phase Diagrams of Ternary Amorphous Alloys* (Springer, 1997).
104. Gao, M. C., Yeh, J. W., Liaw, P. K. & Zhang, Y. *High-Entropy Alloys: Fundamentals and Applications* (Springer, 2016).
105. Miracle, D. B. High entropy alloys as a bold step forward in alloy development. *Nat. Commun.* **10**, 1805 (2019).
106. George, E. P., Raabe, D. & Ritchie, R. O. High-entropy alloys. *Nat. Rev. Mater.* **4**, 515–534 (2019).
107. Yeh, J.-W. et al. Nanostructured high-entropy alloys with multiple principle elements: Novel alloy design concepts and outcomes. *Adv. Eng. Mater.* **6**, 299–303 (2004).
108. Cantor, B., Chang, I. T. H., Knight, P. & Vincent, A. J. B. Microstructural development in equiatomic multicomponent alloys. *Mater. Sci. Eng. A* **375–377**, 213–218 (2004).
109. Senkov, O. N., Miller, J. D., Miracle, D. B. & Woodward, C. Accelerated exploration of multi-principal element alloys with solid solution phases. *Nat. Commun.* **6**, 6529 (2015).
110. Gorsev, S., Miracle, D. B. & Senkov, O. N. Mapping the world of complex concentrated alloys. *Acta Mater.* **135**, 177–187 (2017).
111. Gludovatz, B. et al. A fracture-resistant high-entropy alloy for cryogenic applications. *Science* **345**, 1153–1158 (2014).
112. Li, Z., Pradeep, K. G., Deng, Y., Raabe, D. & Tasan, C. C. Metastable high-entropy dual-phase alloys overcome the strength–ductility trade-off. *Nature* **534**, 227–230 (2016).
113. Li, Z., Tasan, C. C., Springer, H., Gault, B. & Raabe, D. Interstitial atoms enable joint twinning and transformation induced plasticity in strong and ductile high-entropy alloys. *Sci. Rep.* **7**, 40704 (2017).
114. Islam, N., Huang, W. & Zhuang, H. L. Machine learning for phase selection in multi-principal element alloys. *Comput. Mater. Sci.* **150**, 230–235 (2018).
115. Huang, W., Martin, P. & Zhuang, H. L. Machine-learning phase prediction of high-entropy alloys. *Acta Mater.* **169**, 225–236 (2019).
116. Zhang, Y. M., Yang, S. & Evans, J. R. G. Revisiting Hume-Rothery's rules with artificial neural networks. *Acta Mater.* **56**, 1094–1105 (2008).
117. Nong, Z.-S. et al. Stability and structure prediction of cubic phase in as cast high entropy alloys. *Mater. Sci. Technol.* **30**, 363–369 (2014).
118. Jiang, X., Zhang, R., Zhang, C., Yin, H. & Qu, X. Fast prediction of the quasi phase equilibrium in phase field model for multicomponent alloys based on machine learning method. *Calphad* **66**, 101644 (2019).
119. Tancre, F., Toda-Caraballo, I., Menou, E. & Rivera Diaz-Del-Castillo, P. E. J. Designing high entropy alloys employing thermodynamics and gaussian process statistical analysis. *Mater. Des.* **115**, 486–497 (2017).
120. Menou, E. et al. Evolutionary design of strong and stable high entropy alloys using multi-objective optimisation based on physical models, statistics and thermodynamics. *Mater. Des.* **143**, 185–195 (2018).
121. Li, Y. & Guo, W. Machine-learning model for predicting phase formations of high-entropy alloys. *Phys. Rev. Mater.* **3**, 095005 (2019).
122. Abu-Odeh, A. et al. Efficient exploration of the High Entropy Alloy composition-phase space. *Acta Mater.* **152**, 41–57 (2018).
123. Asensi Domínguez, L., Goodall, R. & Todd, I. Prediction and validation of quaternary high entropy alloys using statistical approaches. *Mater. Sci. Technol.* **31**, 1201–1206 (2015).
124. Qi, J., Cheung, A. M. & Poon, S. J. High entropy alloys mined from binary phase diagrams. *Sci. Rep.* **9**, 15501 (2019).
125. Dai, D. et al. Using machine learning and feature engineering to characterize limited material datasets of high-entropy alloys. *Comput. Mater. Sci.* **175**, 109618 (2020).
126. Miracle, D. B. & Senkov, O. N. A critical review of high entropy alloys and related concepts. *Acta Mater.* **122**, 448–511 (2017).
127. Lederer, Y., Toher, C., Vecchio, K. S. & Curtarolo, S. The search for high entropy alloys: A high-throughput ab-initio approach. *Acta Mater.* **159**, 364–383 (2018).
128. Menou, E. et al. Computational design of light and strong high entropy alloys (HEA): Obtaining of an extremely high specific solid solution hardening. *Scr. Mater.* **156**, 120–123 (2018).
129. Kaufmann, K. et al. Discovery of high-entropy ceramics via machine learning. *NPJ Comput. Mater.* **6**, 42 (2020).
130. Zhang, Y. et al. Phase prediction in high entropy alloys with a rational selection of materials descriptors and machine learning models. *Acta Mater.* **185**, 528–539 (2020).
131. Shapeev, A. Accurate representation of formation energies of crystalline alloys with many components. *Comput. Mater. Sci.* **139**, 26–30 (2017).
132. Grabowski, B. et al. Ab initio vibrational free energies including anharmonicity for multicomponent alloys. *NPJ Comput. Mater.* **5**, 80 (2019).
133. Zhang, J. et al. Robust data-driven approach for predicting the configurational energy of high entropy alloys. *Mater. Des.* **185**, 108247 (2020).
134. Kostiluchenko, T., Körmann, F., Neugebauer, J. & Shapeev, A. Impact of lattice relaxations on phase transitions in a high-entropy alloy studied by machine-learning potentials. *NPJ Comput. Mater.* **5**, 55 (2019).
135. Meshkov, E. A., Novoselov, I. I., Shapeev, A. V. & Yanilkin, A. V. Sublattice formation in CoCrFeNi high-entropy alloy. *Intermetallics* **112**, 106542 (2019).
136. Jafary-Zadeh, M., Khoo, K. H., Laskowski, R., Branicio, P. S. & Shapeev, A. V. Applying a machine learning interatomic potential to unravel the effects of local lattice distortion on the elastic properties of multi-principal element alloys. *J. Alloy. Compd.* **803**, 1054–1062 (2019).
137. Li, X.-G., Chen, C., Zheng, H., Zuo, Y. & Ong, S. P. Complex strengthening mechanisms in the NbMoTaW multi-principal element alloy. *NPJ Comput. Mater.* **6**, 70 (2020).
138. Wen, C. et al. Machine learning assisted design of high entropy alloys with desired property. *Acta Mater.* **170**, 109–117 (2019).
139. Kim, G. et al. First-principles and machine learning predictions of elasticity in severely lattice-distorted high-entropy alloys with experimental validation. *Acta Mater.* **181**, 124–138 (2019).
140. Chang, Y.-J., Jui, C.-Y., Lee, W.-J. & Yeh, A.-C. Prediction of the composition and hardness of high-entropy alloys by machine learning. *JOM* **71**, 3433–3442 (2019).
141. Rickman, J. M. et al. Materials informatics for the screening of multi-principal elements and high-entropy alloys. *Nat. Commun.* **10**, 2618 (2019).
142. Wu, Q. et al. Uncovering the eutectics design by machine learning in the Al–Co–Cr–Fe–Ni high entropy system. *Acta Mater.* **182**, 278–286 (2020).
143. Batchelor, T. A. A. et al. High-entropy alloys as a discovery platform for electrocatalysis. *Joule* **3**, 834–845 (2019).
144. Xue, D. et al. Accelerated search for materials with targeted properties by adaptive design. *Nat. Commun.* **7**, 11241 (2016).
145. Copakumar, A. M., Balachandran, P. V., Xue, D., Gubernatis, J. E. & Lookman, T. Multi-objective optimization for materials discovery via adaptive design. *Sci. Rep.* **8**, 3738 (2018).
146. Solorou, A. et al. Multi-objective Bayesian materials discovery: Application on the discovery of precipitation strengthened NiTi shape memory alloys through micromechanical modeling. *Mater. Des.* **160**, 810–827 (2018).

147. Xue, D. et al. An informatics approach to transformation temperatures of NiTi-based shape memory alloys. *Acta Mater.* **125**, 532–541 (2017).
148. Mahmoudi, M. et al. On the printability and transformation behavior of nickel-titanium shape memory alloys fabricated using laser powder-bed fusion additive manufacturing. *J. Manuf. Process.* **35**, 672–680 (2018).
149. Dehghanmehrasi, R. et al. Optimal experimental design for materials discovery. *Comput. Mater. Sci.* **129**, 311–322 (2017).
150. Jiang, X. et al. An materials informatics approach to Ni-based single crystal superalloys lattice misfit prediction. *Comput. Mater. Sci.* **143**, 295–300 (2018).
151. Tancret, F. Computational thermodynamics, Gaussian processes and genetic algorithms: combined tools to design new alloys. *Model. Simul. Mater. Sci. Eng.* **21**, 045013 (2013).
152. Menou, E., Ramstein, G., Bertrand, E. & Tancret, F. Multi-objective constrained design of nickel-base superalloys using data mining- and thermodynamics-driven genetic algorithms. *Model. Simul. Mater. Sci. Eng.* **24**, 055001 (2016).
153. Conduit, B. D., Jones, N. G., Stone, H. J. & Conduit, G. J. Design of a nickel-base superalloy using a neural network. *Mater. Des.* **131**, 358–365 (2017).
154. Hu, X. et al. Two-way design of alloys for advanced ultra-supercritical plants based on machine learning. *Comput. Mater. Sci.* **155**, 331–339 (2018).
155. Yoshitake, S., Narayan, V., Harada, H., Bhadeshia, H. K. D. H. & Mackay, D. J. C. Estimation of the γ and γ' lattice parameters in nickel-base superalloys using neural network analysis. *ISIJ Int.* **38**, 495–502 (1998).
156. Chandran, M., Lee, S. C. & Shim, J.-H. Machine learning assisted first-principles calculation of multicomponent solid solutions: estimation of interface energy in Ni-based superalloys. *Model. Simul. Mater. Sci. Eng.* **26**, 025010 (2018).
157. Goldsmith, B. R., Esterhazy, J., Liu, J.-X., Bartel, C. J. & Sutton, C. Machine learning for heterogeneous catalyst design and discovery. *AIChE J.* **64**, 2311–2323 (2018).
158. Kitchin, J. R. Machine learning in catalysis. *Nat. Catal.* **1**, 230–232 (2018).
159. Toyao, T. et al. Machine learning for catalysis informatics: Recent applications and prospects. *ACS Catal.* **10**, 2260–2297 (2020).
160. Orupattur, N. V., Mushrif, S. H. & Prasad, V. Catalytic materials and chemistry development using a synergistic combination of machine learning and ab initio methods. *Comput. Mater. Sci.* **174**, 109474 (2020).
161. Logadottir, A. et al. The Bronsted–Evans–Polanyi relation and the volcano plot for ammonia synthesis over transition metal catalysts. *J. Catal.* **197**, 229–231 (2001).
162. Nørskov, J. K. et al. Universality in heterogeneous catalysis. *J. Catal.* **209**, 275–278 (2002).
163. Hammer, B. & Nørskov, J. K. Why gold is the noblest of all the metals. *Nature* **376**, 238–240 (1995).
164. Kitchin, J. R., Nørskov, J. K., Barteau, M. A. & Chen, J. G. Modification of the surface electronic and chemical properties of Pt(111) by subsurface 3d transition metals. *J. Chem. Phys.* **120**, 10240–10246 (2004).
165. Panapitiya, G. et al. Machine-learning prediction of CO adsorption in thiolated, Ag-alloyed Au nanoclusters. *J. Am. Chem. Soc.* **140**, 17508–17514 (2018).
166. Li, Z., Ma, X. & Xin, H. Feature engineering of machine-learning chemisorption models for catalyst design. *Catal. Today* **280**, 232–238 (2017).
167. Li, Z., Wang, S., Chin, W. S., Achenie, L. E. & Xin, H. High-throughput screening of bimetallic catalysts enabled by machine learning. *J. Mater. Chem. A* **5**, 24131–24138 (2017).
168. Ma, X., Li, Z., Achenie, L. E. K. & Xin, H. Machine-learning-augmented chemisorption model for CO₂ electroreduction catalyst screening. *J. Phys. Chem. Lett.* **6**, 3528–3533 (2015).
169. Pankajakshan, P. et al. Machine learning and statistical analysis for materials science: Stability and transferability of fingerprint descriptors and chemical insights. *Chem. Mater.* **29**, 4190–4201 (2017).
170. Toyao, T. et al. Toward effective utilization of methane: Machine learning prediction of adsorption energies on metal alloys. *J. Phys. Chem. C* **122**, 8315–8326 (2018).
171. Andersen, M., Levchenko, S. V., Scheffler, M. & Reuter, K. Beyond scaling relations for the description of catalytic materials. *ACS Catal.* **9**, 2752–2759 (2019).
172. Tran, K. & Ulissi, Z. W. Active learning across intermetallics to guide discovery of electrocatalysts for CO₂ reduction and H₂ evolution. *Nat. Catal.* **1**, 696–703 (2018).
173. Back, S. et al. Convolutional neural network of atomic surface structures to predict binding energies for high-throughput screening of catalysts. *J. Phys. Chem. Lett.* **10**, 4401–4408 (2019).
174. Zhong, M. et al. Accelerated discovery of CO₂ electrocatalysts using active machine learning. *Nature* **581**, 178–183 (2020).
175. Boes, J. R. & Kitchin, J. R. Modeling segregation on AuPd(111) surfaces with density functional theory and Monte Carlo simulations. *J. Phys. Chem. C* **121**, 3479–3487 (2017).
176. Cao, L., Li, C. & Mueller, T. The use of cluster expansions to predict the structures and properties of surfaces and nanostructured materials. *J. Chem. Inf. Model.* **58**, 2401–2413 (2018).
177. Cao, L. & Mueller, T. Rational design of Pt_xNi surface structures for the oxygen reduction reaction. *J. Phys. Chem. C* **119**, 17735–17747 (2015).
178. Cao, L., Niu, L. & Mueller, T. Computationally generated maps of surface structures and catalytic activities for alloy phase diagrams. *Proc. Natl. Acad. Sci. USA* **116**, 22044–22051 (2019).
179. Mueller, T. Ab initio determination of structure-property relationships in alloy nanoparticles. *Phys. Rev. B* **86**, 144201 (2012).
180. Wang, L.-L., Tan, T. L. & Johnson, D. D. Configurational thermodynamics of alloyed nanoparticles with adsorbates. *Nano Lett.* **14**, 7077–7084 (2014).
181. Tan, T. L., Wang, L.-L., Johnson, D. D. & Bai, K. A comprehensive search for stable Pt–Pd nanoalloy configurations and their use as tunable catalysts. *Nano Lett.* **12**, 4875–4880 (2012).
182. Jia, Q. et al. Roles of Mo surface dopants in enhancing the ORR performance of octahedral PtNi nanoparticles. *Nano Lett.* **18**, 798–804 (2018).
183. Cao, L. et al. Differential surface elemental distribution leads to significantly enhanced stability of PtNi-based ORR catalysts. *Matter* **1**, 1567–1580 (2019).
184. Wang, L.-L., Tan, T. L. & Johnson, D. D. Nanoalloy electrocatalysis: simulating cyclic voltammetry from configurational thermodynamics with adsorbates. *Phys. Chem. Chem. Phys.* **17**, 28103–28111 (2015).
185. Li, C. et al. Improved prediction of nanoalloy structures by the explicit inclusion of adsorbates in cluster expansions. *J. Phys. Chem. C* **122**, 18040–18047 (2018).
186. Behler, J. & Parrinello, M. Generalized neural-network representation of high-dimensional potential-energy surfaces. *Phys. Rev. Lett.* **98**, 146401 (2007).
187. Artrith, N. & Kolpak, A. M. Grand canonical molecular dynamics simulations of Cu–Au nanoalloys in thermal equilibrium using reactive ANN potentials. *Comput. Mater. Sci.* **110**, 20–28 (2015).
188. Artrith, N. & Kolpak, A. M. Understanding the composition and activity of electrocatalytic nanoalloys in aqueous solvents: A combination of DFT and accurate neural network potentials. *Nano Lett.* **14**, 2670–2676 (2014).
189. Kang, J. et al. First-principles database driven computational neural network approach to the discovery of active ternary nanocatalysts for oxygen reduction reaction. *Phys. Chem. Chem. Phys.* **20**, 24539–24544 (2018).
190. Hajinazar, S., Sandoval, E. D., Cullo, A. J. & Kolmogorov, A. N. Multitribe evolutionary search for stable Cu–Pd–Ag nanoparticles using neural network models. *Phys. Chem. Chem. Phys.* **21**, 8729–8742 (2019).
191. Jinnochi, R. & Asahi, R. Predicting catalytic activity of nanoparticles by a DFT-aided machine-learning algorithm. *J. Phys. Chem. Lett.* **8**, 4279–4283 (2017).
192. Jäger, M. O. J., Morooka, E. V., Federici Canova, F., Himanen, L. & Foster, A. S. Machine learning hydrogen adsorption on nanoclusters through structural descriptors. *NPJ Comput. Mater.* **4**, 37 (2018).
193. Carrasquilla, J. & Melko, R. G. Machine learning phases of matter. *Nat. Phys.* **13**, 431–434 (2017).
194. van Nieuwenburg, E. P. L., Liu, Y.-H. & Huber, S. D. Learning phase transitions by confusion. *Nat. Phys.* **13**, 435–439 (2017).
195. Kusne, A. G. et al. On-the-fly machine-learning for high-throughput experiments: search for rare-earth-free permanent magnets. *Sci. Rep.* **4**, 6367 (2014).
196. Jha, R., Chakraborti, N., Diercks, D. R., Stebner, A. P. & Ciobanu, C. V. Combined machine learning and CALPHAD approach for discovering processing-structure relationships in soft magnetic alloys. *Comput. Mater. Sci.* **150**, 202–211 (2018).
197. Nelson, J. & Sanvito, S. Predicting the Curie temperature of ferromagnets using machine learning. *Phys. Rev. Mater.* **3**, 104405 (2019).
198. Yoshizawa, Y., Oguma, S. & Yamauchi, K. New Fe-based soft magnetic alloys composed of ultrafine grain structure. *J. Appl. Phys.* **64**, 6044–6046 (1988).
199. Rao, K. P. & Prasad, Y. K. D. V. Neural network approach to flow stress evaluation in hot deformation. *J. Mater. Process. Technol.* **53**, 552–566 (1995).
200. Larkiola, J., Myllykoski, P., Nylander, J. & Korhonen, A. S. Prediction of rolling force in cold rolling by using physical models and neural computing. *J. Mater. Process. Technol.* **60**, 381–386 (1996).
201. Chun, M. S., Biglou, J., Lenard, J. G. & Kim, J. G. Using neural networks to predict parameters in the hot working of aluminum alloys. *J. Mater. Process. Technol.* **86**, 245–251 (1999).
202. Malinov, S., Sha, W. & McKeown, J. J. Modelling the correlation between processing parameters and properties in titanium alloys using artificial neural network. *Comput. Mater. Sci.* **21**, 375–394 (2001).
203. Guo, Z. & Sha, W. Modelling the correlation between processing parameters and properties of managing steels using artificial neural network. *Comput. Mater. Sci.* **29**, 12–28 (2004).
204. Mandal, S., Sivaprasad, P. V., Venugopal, S. & Murthy, K. P. N. Artificial neural network modeling to evaluate and predict the deformation behavior of stainless steel type AISI 304L during hot torsion. *Appl. Soft Comput.* **9**, 237–244 (2009).
205. Sun, Y. et al. Development of constitutive relationship model of Ti60 alloy using artificial neural network. *Comput. Mater. Sci.* **48**, 686–691 (2010).
206. Ji, G., Li, F., Li, O., Li, H. & Li, Z. A comparative study on Arrhenius-type constitutive model and artificial neural network model to predict high-temperature deformation behaviour in Aermet100 steel. *Mater. Sci. Eng. A* **528**, 4774–4782 (2011).
207. Haghdiari, N., Zarei-Hanzaki, A., Khalesian, A. R. & Abedi, H. R. Artificial neural network modeling to predict the hot deformation behavior of an A356 aluminum alloy. *Mater. Des.* **49**, 386–391 (2013).
208. Reddy, N. S., Panigrahi, B. B., Ho, C. M., Kim, J. H. & Lee, C. S. Artificial neural network modeling on the relative importance of alloying elements and heat treatment temperature to the stability of α and β phase in titanium alloys. *Comput. Mater. Sci.* **107**, 175–183 (2015).
209. Gavard, L., Bhadeshia, H. K. D. H., MacKay, D. J. C. & Suzuki, S. Bayesian neural network model for austenite formation in steels. *Mater. Sci. Technol.* **12**, 453–463 (1996).
210. Bailer-Jones, C. A. L., Bhadeshia, H. K. D. H. & MacKay, D. J. C. Gaussian process modelling of austenite formation in steel. *Mater. Sci. Technol.* **15**, 287–294 (1999).
211. Capdevila, C., Caballero, F. G. & García de Andrés, C. Determination of Ms temperature in steels: A Bayesian neural network model. *ISIJ Int.* **42**, 894–902 (2002).
212. Capdevila, C., Caballero, F. G. & García de Andrés, C. Analysis of effect of alloying elements on martensite start temperature of steels. *Mater. Sci. Technol.* **19**, 581–586 (2003).
213. Davies, R. H., Dinsdale, A. T., Gisby, J. A., Robinson, J. A. J. & Martin, S. M. MTDATA — thermodynamic and phase equilibrium software from the national physical laboratory. *Calphad* **26**, 229–271 (2002).
214. Tapia, G., Elwany, A. H. & Sang, H. Prediction of porosity in metal-based additive manufacturing using spatial Gaussian process models. *Addit. Manuf.* **12**, 282–290 (2016).
215. Tapia, G., Khairallah, S., Matthews, M., King, W. E. & Elwany, A. Gaussian process-based surrogate modeling framework for process planning in laser powder-bed fusion additive manufacturing of 316L stainless steel. *Int. J. Adv. Manuf. Technol.* **94**, 3591–3603 (2018).
216. Meng, L. & Zhang, J. Process design of laser powder bed fusion of stainless steel using a Gaussian process-based machine learning model. *JOM* **72**, 420–428 (2020).
217. Boyce, B. L. & Uchic, M. D. Progress toward autonomous experimental systems for alloy development. *MRS Bull.* **44**, 273–280 (2019).
218. Ling, J., Hutchinson, M., Antoni, E., Paradiso, S. & Meredig, B. High-dimensional materials and process optimization using data-driven experimental design with well-calibrated uncertainty estimates. *Integr. Mater. Manuf. Innov.* **6**, 207–217 (2017).

219. Godaliyadda, G. M. D. et al. A supervised learning approach for dynamic sampling. *Electron. Imaging* **2016**, *1* (2016).
220. DeCost, B. L., Lei, B., Francis, T. & Holm, E. A. High throughput quantitative metallography for complex microstructures using deep learning: A case study in ultrahigh carbon steel. *Microsc. Microanal.* **25**, 21–29 (2019).
221. Takahashi, K. & Tanaka, Y. Material synthesis and design from first principle calculations and machine learning. *Comput. Mater. Sci.* **112**, 364–367 (2016).
222. Mahfouf, M., Jamei, M. & Linkens, D. A. Optimal design of alloy steels using multiobjective genetic algorithms. *Mater. Manuf. Process.* **20**, 553–567 (2005).
223. Ozerdem, M. S. & Kolukisa, S. Artificial neural network approach to predict mechanical properties of hot rolled, nonresulfurized, AISI 10xx series carbon steel bars. *J. Mater. Process. Technol.* **199**, 437–439 (2008).
224. Ozerdem, M. S. & Kolukisa, S. Artificial neural network approach to predict the mechanical properties of Cu–Sn–Pb–Zn–Ni cast alloys. *Mater. Des.* **30**, 764–769 (2009).
225. Wilk-Kolodziejczyk, D., Regulski, K. & Gumienny, G. Comparative analysis of the properties of the nodular cast iron with carbides and the austempered ductile iron with use of the machine learning and the support vector machine. *Int. J. Adv. Manuf. Technol.* **87**, 1077–1093 (2016).
226. Murugananth, M., Babu, S. S. & David, S. A. Optimization of shielded metal arc weld metal composition for Charpy toughness. *Weld. J.* **83**, 267-S–276-S (2004).
227. Conduit, B. D., Jones, N. G., Stone, H. J. & Conduit, G. J. Probabilistic design of a molybdenum-base alloy using a neural network. *Scr. Mater.* **146**, 82–86 (2018).
228. An, W.-K. et al. Optimization of composition of as-cast chromium white cast iron based on wear-resistant performance. *Mater. Des.* **30**, 2339–2344 (2009).
229. Slavkovic, R., Jugovic, Z., Dragicevic, S., Jovicic, A. & Slavkovic, V. An application of learning machine methods in prediction of wear rate of wear resistant casting parts. *Comput. Ind. Eng.* **64**, 850–857 (2013).
230. Paulson, N. H., Priddy, M. W., McDowell, D. L. & Kalidindi, S. R. Data-driven reduced-order models for rank-ordering the high cycle fatigue performance of polycrystalline microstructures. *Mater. Des.* **154**, 170–183 (2018).
231. Schooling, J. M., Brown, M. & Reed, P. A. S. An example of the use of neural computing techniques in materials science—the modelling of fatigue thresholds in Ni-base superalloys. *Mater. Sci. Eng. A* **260**, 222–239 (1999).
232. Brun, F. et al. Theoretical design of ferritic creep resistant steels using neural network, kinetic, and thermodynamic models. *Mater. Sci. Technol.* **15**, 547–554 (1999).
233. Shin, D., Yamamoto, Y., Brady, M. P., Lee, S. & Haynes, J. A. Modern data analytics approach to predict creep of high-temperature alloys. *Acta Mater.* **168**, 321–330 (2019).
234. Thankachan, T. et al. Artificial neural network to predict the degraded mechanical properties of metallic materials due to the presence of hydrogen. *Int. J. Hydrog. Energy* **42**, 28612–28621 (2017).
235. Rovinelli, A. et al. Assessing reliability of fatigue indicator parameters for small crack growth via a probabilistic framework. *Model. Simul. Mater. Sci. Eng.* **25**, 045010 (2017).
236. Rovinelli, A. et al. Predicting the 3D fatigue crack growth rate of small cracks using multimodal data via Bayesian networks: In-situ experiments and crystal plasticity simulations. *J. Mech. Phys. Solids* **115**, 208–229 (2018).
237. Feng, S., Zhou, H. & Dong, H. Using deep neural network with small dataset to predict material defects. *Mater. Des.* **162**, 300–310 (2019).
238. Gossett, E. et al. AFLOW-ML: A RESTful API for machine-learning predictions of materials properties. *Comput. Mater. Sci.* **152**, 134–145 (2018).
239. Taylor, R. H. et al. A RESTful API for exchanging materials data in the AFLOWLIB.org consortium. *Comput. Mater. Sci.* **93**, 178–192 (2014).
240. Fernandez-Zelaia, P., Joseph, V., Kalidindi, S. R. & Melkote, S. N. Estimating mechanical properties from spherical indentation using Bayesian approaches. *Mater. Des.* **147**, 92–105 (2018).
241. Wisner, B. & Kontos, A. Investigation of particle fracture during fatigue of aluminum 2024. *Int. J. Fatigue* **111**, 33–43 (2018).
242. Chatterjee, S., Murugananth, M. & Bhadeshia, H. K. D. H. δ TRIP steel. *Mater. Sci. Technol.* **23**, 819–827 (2007).
243. Xiong, J., Zhang, T. & Shi, S. Machine learning of mechanical properties of steels. *Sci. China Technol. Sci.* **63**, 1247–1255 (2020).
244. Chaudhary, N., Abu-Odeh, A., Karaman, I. & Arróyave, R. A data-driven machine learning approach to predicting stacking fault energy in austenitic steels. *J. Mater. Sci.* **52**, 11048–11076 (2017).
245. Mangal, A. & Holm, E. A. Applied machine learning to predict stress hotspots I: Face centered cubic materials. *Int. J. Plast.* **111**, 122–134 (2018).
246. Mangal, A. & Holm, E. A. A comparative study of feature selection methods for stress hotspot classification in materials. *Integr. Mater. Manuf. Innov.* **7**, 87–95 (2018).
247. Abbassi, F., Belhadj, T., Mistou, S. & Zghal, A. Parameter identification of a mechanical ductile damage using Artificial Neural Networks in sheet metal forming. *Mater. Des.* **45**, 605–615 (2013).
248. Agrawal, A. et al. Exploration of data science techniques to predict fatigue strength of steel from composition and processing parameters. *Integr. Mater. Manuf. Innov.* **3**, 90–108 (2014).
249. Agrawal, A. & Choudhary, A. An online tool for predicting fatigue strength of steel alloys based on ensemble data mining. *Int. J. Fatigue* **113**, 389–400 (2018).
250. Seko, A., Maekawa, T., Tsuda, K. & Tanaka, I. Machine learning with systematic density-functional theory calculations: Application to melting temperatures of single- and binary-component solids. *Phys. Rev. B* **89**, 054303 (2014).
251. Carrete, J., Li, W., Mingo, N., Wang, S. & Curtarolo, S. Finding unprecedentedly low-thermal-conductivity half-Heusler semiconductors via high-throughput materials modeling. *Phys. Rev. X* **4**, 011019 (2014).
252. Legrain, F., Carrete, J., van Roekeghem, A., Madsen, G. K. H. & Mingo, N. Materials screening for the discovery of new half-Heuslers: Machine learning versus ab initio methods. *J. Phys. Chem. B* **122**, 625–632 (2017).
253. Carrete, J., Mingo, N., Wang, S. & Curtarolo, S. Nanogranular half-Heusler semiconductors as advanced thermoelectrics: An ab initio high-throughput statistical study. *Adv. Func. Mater.* **24**, 7427–7432 (2014).
254. Sparks, T. D., Gaultois, M. W., Oliynyk, A., Brugoch, J. & Meredig, B. Data mining our way to the next generation of thermoelectrics. *Scr. Mater.* **111**, 10–15 (2016).
255. Breiman, L. Random forests. *Mach. Learn.* **45**, 5–32 (2001).
256. Oses, C., Toher, C. & Curtarolo, S. High-entropy ceramics. *Nat. Rev. Mater.* **5**, 295–309 (2020).
257. Sun, S., Ouyang, R., Zhang, B. & Zhang, T.-Y. Data-driven discovery of formulas by symbolic regression. *MRS Bull.* **44**, 559–564 (2019).
258. Hernandez, A., Balasubramanian, A., Yuan, F., Mason, S. A. M. & Mueller, T. Fast, accurate, and transferable many-body interatomic potentials by symbolic regression. *NPJ Comput. Mater.* **5**, 112 (2019).
259. Iten, R., Metger, T., Wilming, H., del Rio, L. & Renner, R. Discovering physical concepts with neural networks. *Phys. Rev. Lett.* **124**, 010508 (2020).
260. Routh, P. K., Liu, Y., Marcella, N., Kozinsky, B. & Frenkel, A. I. Latent representation learning for structural characterization of catalysts. *J. Phys. Chem. Lett.* **12**, 2086–2094 (2021).
261. Schmidt, J., Benavides-Riveros, C. L. & Marques, M. A. L. Machine learning the physical nonlocal exchange–correlation functional of density-functional theory. *J. Phys. Chem. Lett.* **10**, 6425–6431 (2019).
262. Lei, X. & Medford, A. J. Design and analysis of machine learning exchange–correlation functionals via rotationally invariant convolutional descriptors. *Phys. Rev. Mater.* **3**, 063801 (2019).
263. Kalita, B., Li, L., McCarty, R. J. & Burke, K. Learning to approximate density functionals. *Acc. Chem. Res.* **54**, 818–826 (2021).
264. Dick, S. & Fernandez-Serra, M. Machine learning accurate exchange and correlation functionals of the electronic density. *Nat. Commun.* **11**, 3509 (2020).
265. Andersen, C. W. et al. OPTIMADE: an API for exchanging materials data. Preprint at [arXiv https://arxiv.org/abs/2103.02068](https://arxiv.org/abs/2103.02068) (2021).
266. Schmitz, G., Godtliebsen, I. H. & Christiansen, O. Machine learning for potential energy surfaces: An extensive database and assessment of methods. *J. Chem. Phys.* **150**, 244113 (2019).
267. Artrith, N., Urban, A. & Ceder, G. Constructing first-principles phase diagrams of amorphous Li_xSi using machine-learning-assisted sampling with an evolutionary algorithm. *J. Chem. Phys.* **148**, 241711 (2018).
268. Mueller, T., Johlin, E. & Grossman, J. C. Origins of hole traps in hydrogenated nanocrystalline and amorphous silicon revealed through machine learning. *Phys. Rev. B* **89**, 115202 (2014).
269. Yang, K., Oses, C. & Curtarolo, S. Modeling off-stoichiometry materials with a high-throughput ab initio approach. *Chem. Mater.* **28**, 6484–6492 (2016).
270. Okhotnikov, K., Charpentier, T. & Cadars, S. Supercell program: a combinatorial structure-generation approach for the local-level modeling of atomic substitutions and partial occupancies in crystals. *J. Cheminform.* **8**, 17 (2016).
271. Kikuchi, R. A theory of cooperative phenomena. *Phys. Rev.* **81**, 988 (1951).
272. Sanchez, J. M. & de Fontaine, D. The fcc Ising model in the cluster variation approximation. *Phys. Rev. B* **17**, 2926 (1978).
273. Zhang, Y., Blum, V. & Reuter, K. Accuracy of first-principles lateral interactions: Oxygen at Pd(100). *Phys. Rev. B* **75**, 235406 (2007).
274. Stampfli, C., Kreuzer, H. J., Payne, S. H., Pfür, H. & Scheffler, M. First-principles theory of surface thermodynamics and kinetics. *Phys. Rev. Lett.* **83**, 2993 (1999).
275. Fichthorn, K. A., Merrick, M. L. & Scheffler, M. A kinetic Monte Carlo investigation of island nucleation and growth in thin-film epitaxy in the presence of substrate-mediated interactions. *Appl. Phys. A* **75**, 17–23 (2002).
276. Connolly, J. W. D. & Williams, A. R. Density-functional theory applied to phase transformations in transition-metal alloys. *Phys. Rev. B* **27**, 5169 (1983).
277. Blum, V., Hart, G. L. W., Walorski, M. J. & Zunger, A. Using genetic algorithms to map first-principles results to model Hamiltonians: Application to the generalized Ising model for alloys. *Phys. Rev. B* **72**, 165113 (2005).
278. Seko, A. et al. First-principles study of cation disordering in MgAl₂O₄ spinel with cluster expansion and Monte Carlo simulation. *Phys. Rev. B* **73**, 094116 (2006).
279. Van der Ven, A., Thomas, J. C., Xu, Q., Swoboda, B. & Morgan, D. Nondilute diffusion from first principles: Li diffusion in Li_xTi₂. *Phys. Rev. B* **78**, 104306 (2008).
280. Laks, D. B., Ferreira, L., Froyen, S. & Zunger, A. Efficient cluster expansion for substitutional systems. *Phys. Rev. B* **46**, 12587 (1992).
281. Mueller, T. & Ceder, G. Bayesian approach to cluster expansions. *Phys. Rev. B* **80**, 024103 (2009).
282. Cockayne, E. & van de Walle, A. Building effective models from sparse but precise data: Application to an alloy cluster expansion model. *Phys. Rev. B* **81**, 012104 (2010).
283. Nelson, L. J., Ozolinš, V., Reese, C. S., Zhou, F. & Hart, G. L. W. Cluster expansion made easy with Bayesian compressive sensing. *Phys. Rev. B* **88**, 155105 (2013).
284. Zunger, A., Wang, L. G., Hart, G. L. W. & Sanati, M. Obtaining Ising-like expansions for binary alloys from first principles. *Model. Simul. Mater. Sci. Eng.* **10**, 685 (2002).
285. Hart, G. L. W. & Forcade, R. W. Algorithm for generating derivative structures. *Phys. Rev. B* **77**, 224115 (2008).
286. Seko, A., Togo, A., Oba, F. & Tanaka, I. Structure and stability of a homologous series of tin oxides. *Phys. Rev. Lett.* **100**, 045702 (2008).
287. Seko, A., Koyama, Y. & Tanaka, I. Cluster expansion method for multicomponent systems based on optimal selection of structures for density-functional theory calculations. *Phys. Rev. B* **80**, 165122 (2009).
288. Mueller, T. & Ceder, G. Exact expressions for structure selection in cluster expansions. *Phys. Rev. B* **82**, 184107 (2010).
289. van de Walle, A. & Ceder, G. First-principles computation of the vibrational entropy of ordered and disordered Pd₃V. *Phys. Rev. B* **61**, 5972 (2000).
290. Nguyen, A. H., Rosenbrock, C. W., Reese, C. S. & Hart, G. L. W. Robustness of the cluster expansion: Assessing the roles of relaxation and numerical error. *Phys. Rev. B* **96**, 014107 (2017).
291. Daw, M. S. & Baskes, M. I. Semiempirical quantum mechanical calculation of hydrogen embrittlement in metals. *Phys. Rev. Lett.* **50**, 1285 (1983).
292. van der Oord, C., Duuson, G., Csányi, G. & Ortner, C. Regularised atomic body-ordered permutation-invariant polynomials for the construction of interatomic potentials. *Mach. Learn. Sci. Technol.* **1**, 015004 (2020).

293. Drautz, R. Atomic cluster expansion of scalar, vectorial, and tensorial properties including magnetism and charge transfer. *Phys. Rev. B* **102**, 024104 (2020).
294. Dusson, G. et al. Atomic cluster expansion: Completeness, efficiency and stability. Preprint at *arXiv* <https://arxiv.org/abs/1911.03550> (2019).
295. Willatt, M. J., Musil, F. & Ceriotti, M. Atom-density representations for machine learning. *J. Chem. Phys.* **150**, 154110 (2019).
296. Seko, A. Machine learning potentials for multicomponent systems: The Ti-Al binary system. *Phys. Rev. B* **102**, 174104 (2020).
297. Hajinazar, S., Thorn, A., Sandoval, E. D., Kharabadez, S. & Kolmogorov, A. N. MAISE: Construction of neural network interatomic models and evolutionary structure optimization. *Comput. Phys. Commun.* **259**, 107679 (2021).
298. Dolgirev, P. E., Kruglov, I. A. & Oganov, A. R. Machine learning scheme for fast extraction of chemically interpretable interatomic potentials. *AIP Adv.* **6**, 085318 (2016).
299. Brown, W. M., Thompson, A. P. & Schultz, P. A. Efficient hybrid evolutionary optimization of interatomic potential models. *J. Chem. Phys.* **132**, 024108 (2010).
300. Slepoy, A., Peters, M. D. & Thompson, A. P. Searching for globally optimal functional forms for interatomic potentials using genetic programming with parallel tempering. *J. Comput. Chem.* **28**, 2465–2471 (2007).
301. Kenoufi, A. & Holmurodov, K. T. Symbolic regression of interatomic potentials via genetic programming. *Biol. Chem. Res.* **2**, 1–10 (2015).
302. Makarov, D. E. & Metiu, H. Fitting potential-energy surfaces: a search in the function space by directed genetic programming. *J. Chem. Phys.* **108**, 590–598 (1998).
303. Unke, O. T. & Meuwly, M. PhysNet: A neural network for predicting energies, forces, dipole moments, and partial charges. *J. Chem. Theory Comput.* **15**, 3678–3693 (2019).
304. Gilmer, J., Schoenholz, S. S., Riley, P. F., Vinyals, O. & Dahl, G. E. Neural message passing for quantum chemistry. *Proc. Mach. Learn. Res.* **70**, 1263–1272 (2017).
305. Duvenaud, D. et al. in *Proceedings of Advances in Neural Information Processing Systems* Vol. 28, 2224–2232 (2015).
306. Kearnes, S., McCloskey, K., Berndl, M., Pande, V. & Riley, P. Molecular graph convolutions: moving beyond fingerprints. *J. Comput. Aided Mol. Des.* **30**, 595–608 (2016).
307. Jorgensen, P. B., Jacobsen, K. W. & Schmidt, M. N. in *32nd Conference on Neural Information Processing Systems* (Elsevier, 2018).
308. Rosenbrock, C. W. et al. Machine-learned interatomic potentials for alloys and alloy phase diagrams. *NPJ Comput. Mater.* **7**, 24 (2021).
309. Gubaev, K., Podryabinikin, E. V., Hart, G. L. W. & Shapeev, A. V. Accelerating high-throughput searches for new alloys with active learning of interatomic potentials. *Comput. Mater. Sci.* **156**, 148–156 (2019).
310. Mueller, T., Hernandez, A. & Wang, C. Machine learning for interatomic potential models. *J. Chem. Phys.* **152**, 050902 (2020).
311. Nyshadham, C. et al. Machine-learned multi-system surrogate models for materials prediction. *NPJ Comput. Mater.* **5**, 51 (2019).
312. Zuo, Y. et al. Performance and cost assessment of machine learning interatomic potentials. *J. Phys. Chem. A* **124**, 731–745 (2020).
313. Pettifor, D. G. A chemical scale for crystal-structure maps. *Solid State Commun.* **51**, 31–34 (1984).
314. Pettifor, D. G. The structures of binary compounds. I. Phenomenological structure maps. *J. Phys. C Solid State Phys.* **19**, 285 (1986).
315. Pettifor, D. G. Structure maps revisited. *J. Phys. Condens. Matter* **15**, V13 (2003).
316. Levy, O., Hart, G. L. W. & Curtarolo, S. Structure maps for hcp metals from first-principles calculations. *Phys. Rev. B* **81**, 174106 (2010).
317. Zunger, A. Systematization of the stable crystal structure of all AB-type binary compounds: A pseudopotential orbital-radii approach. *Phys. Rev. B* **22**, 5839 (1980).
318. Zunger, A. in *Structure and Bonding in Crystals* Ch. 5 (eds O'Keeffe, M. & Navrotsky, A.) 73–135 (Academic Press, 1981).
319. Martynov, A. I. & Batsanov, S. S. New approach to the determination of atom electronegativity. *Zh. Neorg. Khim.* **25**, 3171–3175 (1980).
320. Villars, P. in *Crystal Structures of Intermetallic Compounds* (eds Westbrook, J. H. & Fleischer, R. L.) 1–49 (Wiley, 2000).

Acknowledgements

The authors thank Luca Ghiringhelli, Aleksey Kolmogorov, Axel van de Walle, Atsuto Seko, Chris Wolverton, Karsten Reuter, Anton Van der Ven, Corey Oses, Ohad Levy, Mike Mehl and Xiomara Campilongo for valuable discussions. The authors thank Liang Cao for providing Fig. 4b. T.M. acknowledges support by DOD-ONR (N00014-15-1-2681). C.T. acknowledges support by NSF (DMR-1921909). S.C. and C.T. acknowledge support by DOD-ONR (N00014-15-1-2863, N00014-16-1-2326, N00014-17-1-2876).

Author contributions

All authors contributed equally to the article.

Competing interests

The authors declare no competing interests.

Peer review information

Nature Reviews Materials thanks Vladan Stevanovic, Tong-Yi Zhang and the other, anonymous, reviewer(s) for their contribution to the peer review of this work.

Publisher's note

Springer Nature remains neutral with regard to jurisdictional claims in published maps and institutional affiliations.

© Springer Nature Limited 2021